UNIVERSITY OF OKLAHOMA

GRADUATE COLLEGE

STUDY OF THE LEAD MONOFLUORIDE MOLECULE IN PREPARATION OF A MEASUREMENT OF THE ELECTRIC DIPOLE MOMENT OF THE ELECTRON

A DISSERTATION

SUBMITTED TO THE GRADUATE FACULTY

in partial fullfillment of the requirements for the

degree of

DOCTOR OF PHILOSOPHY

By

CHRISTOPHER PATRICK MCRAVEN
Norman, Oklahoma
2010

STUDY OF THE LEAD MONOFLUORIDE MOLECULE IN PREPARATION OF A MEASUREMENT OF THE ELECTRIC DIPOLE MOMENT OF THE ELECTRON

A DISSERTATION APPROVED FOR THE
HOMER L. DODGE DEPARTMENT OF PHYSICS AND ASTRONOMY

BY

Dr. Neil E. Shafer-Ray, Chair

Dr. Eric R. I. Abraham

Dr. Ron Kantowski

Dr. Douglas Mock

Dr. John Moore-Furneaux

This dissertation is dedicated to my grandfather,

who inspired and encouraged me to study science

and whose unwavering love for

and depth of dedication to his family has always humbled me.

Acknowledgements

I wish to express my gratitude to the many people who supported the completion of this body of work. Thank you all for providing such a great atmosphere in which to do science.

My sincere thanks to my laboratory partner, Dr. Sivakumar Poopalasingam. We worked side by side from the start, and none of this work would have been possible without his contributions and friendship.

I would also like to acknowledge the professional staff of the department for their support of this research. Much of our experimental apparatus was designed, manufactured, and constructed with the help of the highly skilled hands and clever minds of Joel Young, Barry Bergeron, Sean Attebury, and the late Bob Littell. The development of the electronics of our experiment was done with the support and expertise of Adrienne Wade. Thanks to the members of the front office, Debbie Barnhill, Danette Loyd, and Sharon Widner, who face daily the difficult task of maintaining a smoothly running department.

I would like to thank my family and friends for their personal support throughout my education. I am grateful to my mother, father, brother, and grandparents for their faith and patience. Also, I am certain that I would not be where I am today without the love and encouragement of my best friend and partner, Leah Trafford. She has been nothing but sunshine in my life. To her parents, Ross and Vickie Trafford, I am ever grateful for their invaluable assistance and support for the past few years.

I owe my deep gratitude to Dr. Eric Abraham, Dr. Trevor Sears, and Dr. Greg

Hall for their contributions to the analysis and interpretation of our data, as well as their mentorship and friendship. Their personal support was crucial to my success as a graduate student.

Finally, I would like to thank my advisor and mentor Dr. Neil Shafer-Ray for accepting me into his group so many years ago and for shepherding me along this path to a Ph.D. I am forever indebted to him for his dedication to me.

Table of Contents

List of Tables

List of Figures

Abstract

The electric dipole moment of the electron (e-EDM) has important consequences in fundamental theories of matter. Since it was first suggested by Purcell and Ramsey in 1950, it has been pursued in large particle accelerators and table-top atomic beam experiments. The most stringent limit on the upper bound of the e-EDM ($|\vec{p}| < 1.6 \times 10^{-27}\,\mathrm{e} \cdot \mathrm{cm}$) was placed by a series of Thallium atomic beam experiments of Commins and coworkers between 1990 and 2002.

As early as 1975 Sandars realized that certain heavy polar diatomic molecules offer orders of magnitude greater intrinsic sensitivity to the e-EDM than do atoms. However, molecules introduce many new challenges over atoms, including difficulties in production, state dilution, and detection. For this reason, molecular e-EDM measurements are only now beginning to compete with atomic measurements. This dissertation addresses the difficulty of detection of the e-EDM-sensitive lead monofluoride molecule and presents the results of studies that characterize the spectroscopy of the molecule. In all, over 30 spectroscopic parameters have been measured, covering electronic, fine, and hyperfine interactions. These measurements are essential for optimizing detection, analyzing systematic errors and interference from other states, and designing a Ramsey technique for, ultimately, the measurement of the e-EDM.

Chapter 1

Introduction

In grade school we learn of a subatomic particle called the electron that has definite charge and mass. In our first chemistry class we are told that electrons also have a property called spin, that is responsible for allowing two and only two electrons in each atomic suborbital. Later we may learn that the electron has a magnetic dipole moment that is proportional to its spin and describes the strength of its interaction with magnetic fields. Thus it is commonly understood that electrons have charge, mass, spin, and a magnetic dipole moment proportional to spin. It is not, however, common knowledge that electrons are also believed to have another property, namely an electric dipole moment that causes the electric field lines to alter from the radial direction at a very short length scales. This property, first suggest by Purcell and Ramsey [1], has since worked its way into all theories of particle physics.

A curious feature of this postulated property is that, like the magnetic dipole moment, the electric dipole moment must be proportional to spin. If this were not the case, the electron would have another discrete property (or quantum number), and more than two electrons would be allowed in each atomic suborbital, altering the periodic table as we know it. The existence of an electric dipole moment proportional to spin has immediate and profound consequences. Most strikingly, an electric dipole moment breaks time-reversal symmetry of the interaction of an electron with an electromagnetic field.

It's obvious that a recording of a candle burning played in reverse looks unphysical. But in the absence of any processes which increase entropy, there is no reason to believe that physics should behave differently. If a process occurs in accordance to a set of physical laws that exhibit time reversal symmetry, the time reversed ($t \to -t$) process must also obey those laws. As an example of a time symmetric law, consider creating a video of the simple act of tossing a ball in the air and catching it. The motion of the ball obeys the time-symmetric law $F = ma$ and, as a result, one would be hard pressed to distinguish whether a video of the process was being played backward or forward. On the other hand, it is obvious that the recording of a candle burning played in reverse looks unphysical; wax does not steadily flow up from a disorderly puddle to a smooth candle.

To see how the existence of an electric dipole moment creates a time-reversal asymmetry, recall that both the magnetic ($\vec{m}$) and the hypothesized electric ($\vec{p}$) dipole moments must be proportional to spin. Let us label the constants of proportionality a and a_{EDM} respectively. An electron in a parallel magnetic ($\vec{B} = B_0\hat{z}$) and electric ($\vec{E} = E_0\hat{z}$) field will have two energy levels with energies determined by

$$U = \left(-\vec{m} \cdot \vec{B}\right) + \left(-\vec{p} \cdot \vec{E}\right) \tag{1.1}$$

$$= aS_zB_0 + a_{EDM}S_zE_0 \tag{1.2}$$

Here S_z is the spin angular momentum of the electron with $S_z = +\hbar/2$ for the "spin up" state and $S_z = -\hbar/2$ for the "spin down" state. The energy difference between the spin up and spin down state is simply

$$\Delta U = U_{up} - U_{down} = (a_{EDM} E_0 + aB_0)\hbar \tag{1.3}$$

Now imagine an electron in such a parallel electric and magnetic field is in the upper energy (spin $+\hbar/2$) state. According to Einstein's laws, it will eventually emit a photon of energy equal to this energy difference $|\Delta U|$. Because of the electric dipole moment, this emission process, viewed in reverse, is unphysical. This is because the direction of an electric field does not change under time reversal, but both the direction of the magnetic field and the spin do. Thus we have

$$|\Delta U|_{t\to -t} = |(-a_{EDM} E_0 + aB_0)| \neq |\Delta U| \tag{1.4}$$

As a result, in a video playback, one would observe a system changing state by an energy $|\Delta U|_{t\to -t}$, but emitting a photon of energy ΔU, violating conservation of energy. This time-reversed process is just as unphysical as a candle burning backwards. Thus the existence of an e-EDM leads to physical interactions that break time reversal symmetry.

Time-reversal asymmetry, or $\mathcal{T}$-violation, plays a vital role in new theories of particle physics. The current and most successful theory which encompasses all of the known particles of our universe, the Standard Model, fails to explain some mysteries of our universe such as the matter - antimatter asymmetry, "dark" mass and energy, and the hierarchy of masses of quarks and leptons. $\mathcal{T}$-violation could partly explain the matter-antimatter asymmetry in the universe [2]. Although it has been observed in the K_2^0 meson decay [3], this sole source of $\mathcal{T}$-violation is not sufficient. Theories which seek to supersede the Standard Model predict that the existence of an e-EDM could be sufficient to account for the asymmetry. Each competitive new theory predicts the e-EDM to have a different magnitude [4], and the Standard Model itself predicts the e-EDM to be so small that it is essentially unmeasurable [5]. This is where, as Purcell and Ramsey put it, the e-EDM "becomes a purely experimental matter."

The current limit on the upper bounds of the e-EDM ($|\vec{p}| < 1.6 \times 10^{-27}\,\mathrm{e \cdot cm}$) were placed by the Thallium atomic beam experiment of Commins and coworkers between 1990 and 2002 [6, 7, 8]. To give a sense of scale for the size of this measurement of the e-EDM[1], if we zoomed in so that the electron were the size of a ping pong ball, then a ping pong ball would be as large as our universe. The Standard Model predicts the magnitude of the e-EDM to be many orders of magnitude smaller than that ($10^{-38} - 10^{-40}\,\mathrm{e \cdot cm}$) [5]. Even in the largest uniform electric field that can be created in the laboratory ($200\,\mathrm{kV/cm}$), the energy difference, $2\,p\,E$, between a spin-up and spin-down electron is extremely small ($10^{-9}\,\mathrm{Hz}/h$ for $p = 10^{-27}\,\mathrm{e \cdot cm}$.) Sandars showed in 1964 [11] and 1975 [12] that the relativistic motion of an electron in a bound state in atom or molecule samples the very large internal electric fields. Due to this, several heavy atoms and diatomic molecules offer several orders of magnitude better sensitivity to the e-EDM then would a free electron. Heavy atoms and molecules offer another advantage: they can be electrically neutral, preventing rapid acceleration of the system by the electric field.

---

[1] The EDM-length scale of a charged particle p/e gives the length at which field lines no longer emanate radially from the particle. This is distinct from other length scales, such as those defined from corrections from pure Coulomb scattering [9, 10].

In order to measure an e-EDM in an atomic or molecular system, one first must detect the atom or molecule with complete quantum state resolution. When this is achieved, one can compare the energy of two quantum states that differ only by the orientation of rotation about an electric field (cf. Eqns. (1.4)). Time-reversal symmetry guarantees that these energies will be degenerate. For favorable atoms and molecules, the existence of even a very small e-EDM will break this symmetry leading to a measurable energy difference between the states.

The sensitivity of Thallium to the e-EDM is such that if the e-EDM had a value of $1.6 \times 10^{-27}\,\mathrm{e \cdot cm}$, the corresponding shift in energy would be approximately $30\,\mu\mathrm{Hz}$. The experiment of Commins and coworkers attempted to measure such a tiny shift in energy, and the experiment was ultimately limited by systematic errors. Many heavy diatomic molecules have even larger sensitivities to the e-EDM and do not suffer from the same systematic errors [13, 14, 15, 16]. Among these, lead monofluoride is a strong candidate for this measurement for four reasons. First, PbF has been calculated to have an excellent sensitivity to the e-EDM [17, 18, 15]. At the current Thallium-set limit on the e-EDM, the corresponding energy shift in the PbF molecule would be $10,000\,\mu\mathrm{Hz}$. Second, the interaction of the valence electron in the electronic ground state has been shown to be insensitive to external magnetic fields [19], a cause of systematic errors. Thirdly, the large polarizability of the PbF molecule implies only a modest ($\sim 1\,\mathrm{kV/cm}$) field is required to gain sensitivity to the e-EDM. Lastly, it is the ground electronic state that is sensitive to the e-EDM. For many of the molecules sensitive to the e-EDM, it is an excited state that is sensitive. This simplifies production and state preparation and, more importantly, allows for a linewidth limited only by the experimental apparatus and not the lifetime of the excited state.

Despite clear advantages, molecules introduce many new challenges over atoms, including difficulties in production of the molecule, state preparation of the quantum states that probe the e-EDM, and precise detection of these quantum states. Lead monofluoride itself is a free radical that is highly reactive. Techniques for isolation of free radicals are established, but a high production rate is difficult. Furthermore, diatomic molecules, unlike atoms, can rotate and vibrate. Because of this, the number of quantum states that can be produced is very large, while, as pointed out above, one is concerned with only two of these many quantum states. Finally, fully quantum-state-resolved detection of PbF had never been accomplished at the outset of this experiment in 2006. This thesis describes progress we made to overcome these challenges and leave us on the brink of an e-EDM measurement

The primary challenge that lay head of us was to develop, first, a successful detection scheme and, next, a detection scheme capable of an unprecedented resolution. To this end, we chose to detect the quantum states of PbF using a technique called resonance enhanced multiphoton ionization (REMPI) [20, 21, 22]. REMPI was the most favorable detection scheme due to its 10^2–10^4 improvement in sensitivity over other means, such as laser induced fluorescence and laser absorption [23]. Given that PbF is difficult to produce, a higher detection sensitivity allows for a weaker source. While REMPI offers high sensitivity for probing molecular systems, the state-of-the-art resolution was an order of magnitude larger than necessary for complete quantum state resolution. The best resolution achieved for the PbF molecule was $\Delta\nu \approx 600\,\mathrm{MHz}$, and we require a resolution of $50\,\mathrm{MHz}$ [24] to resolve the quantum states. What's more, no e-EDM sensitive molecule had been observed using REMPI.

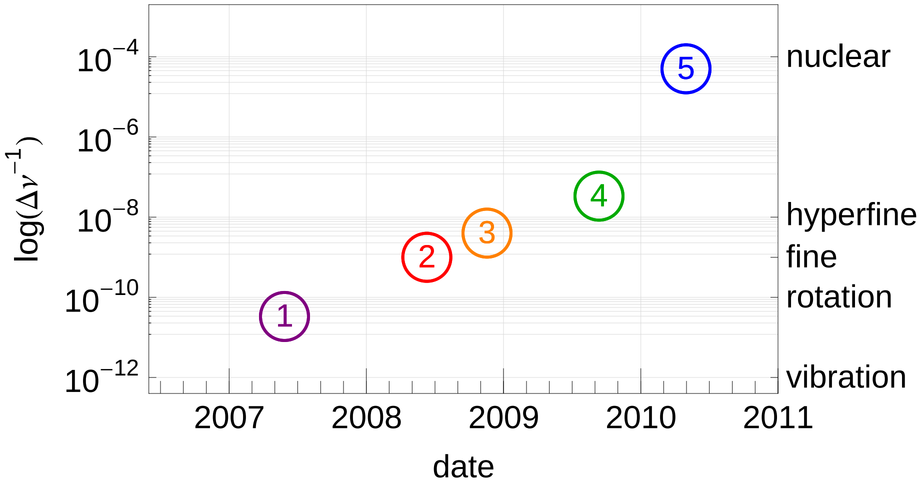

Figure 1.1: Progress of the sensitivity of detection of PbF. Each point on the graph represents a new level of precision and sensitivity, and labeled points are chapters in this dissertation. The left vertical axis is the logarithm of the inverse of the linewidth obtained in the respective experiment. The right vertical axis marks the corresponding interactions which are revealed. See text for discussion.

Figure 1.1 chronicles the progression of resolution in our development of a REMPI probe of the PbF molecule. As we developed techniques for interrogation of lead monofluoride at finer and finer resolution, our knowledge of the structure of the molecule closely tracked. Point ①, represents the starting point for this dissertation: the first demonstration of REMPI of a molecule sensitive to the e-EDM [25]. Chapter 2 describes the state-selective $1 + 1' + 1''$ REMPI which resolves the electronic, rotational, and fine structure of the ground and excited states of PbF (Point ②.) Chapter 3 describes a modified $1 + 1' + 1''$ REMPI scheme which is used to resolve the hyperfine structure due to the ^{207}Pb nucleus (Point ③.) Chapter 4 describes a coincidence detector design for a new REMPI technique and an experiment which resolves of the hyperfine structure due to the fluorine nucleus. (Point ④.) With the development of this new technique, full quantum state resolution was achieved. Finally, Chapter 5 discusses measurements enabled by this new technique, including a microwave experiment conducted in collaboration that allowed reanalysis of previously taken data (Point ⑤.) Additionally, hyperfine constants of the first excited state are presented. The linewidths achieved in the microwave studies are sufficient for a serious e-EDM measurement. What remains is to combine the high resolution of this measurement with control over electric and magnetic fields.

Chapter 2

Rotationally resolved optical spectroscopy of lead monofluoride

In this chapter, a $1+1'+1''$ resonance enhanced multiphoton ionization scheme [25, 26] reveals the electronic and fine structure of many of the excited states of lead monofluoride (Point ② on Figure 1.1, pg. 7.) This technique is used to explore the known excited states of PbF. New molecular constants are determined for the B, D, E, and F states, as well as the symmetry of the D state and the value of Ω of the F state.

As appears in Journal of Molecular Spectroscopy, Vol. 262, pg. 89–92, 2010.

2.1 Introduction

The electronic states of the lead monofluoride molecule have been investigated intermittently since the first absorption and emission studies of Morgan [27] and Rochester [28, 29] in the late 1930s. Later, higher resolution emission studies conducted by Lumley *et al.* [30], modern laser induced fluorescence studies by Chen *et al.* [31] and Shestakov *et al.* [32], and Fourier transform studies by Ziebarth *et al.* [33] refined knowledge of this heavy, relativistic molecule. These studies were complemented by theoretical studies of Balasubramanian [34] and Das [35] which investigated the large ground-state spin-orbit coupling. Lead monofluoride is particularly interesting because of the predicted large sensitivity of the ground state to an electron electric dipole moment [17] (*e*-EDM) and its small g-factor [19, 36]. This leads to the possibility of a long coherence measurement in an electrostatic trap [37, 38] or beam resonance cavity.

We are interested in the development of sensitive, fully quantum-state resolved ionization detection of PbF and application of this probe to the measurement of the *e*-EDM. After a survey of all the known excited electronic states, we found only the A state has a sufficiently long lifetime to obtain quantum state resolution [25, 26, 39]. However, the high photon energy required to directly ionize the A state causes large numbers of background ions. We are able to minimize the background by exciting first to the A state and then ionizing through an intermediate state [26]. Using this $1 + 1' + 1''$ resonance enhanced multiphoton ionization (REMPI) technique, fully quantum-state resolved spectra at the hyperfine level have been observed [36].

As an added benefit of our multiphoton ionization method, rotationally resolved spectra of the short-lived B, D, E, and F states have been obtained. This would not be possible without the suppression of nearby, lifetime broadened rotational lines through the double-resonant simplification. In this work, we take advantage of this new-found selectivity to determine new spectroscopic constants describing these states. By combining these constants with those of previous workers [29, 30, 33], we form an improved picture of connections between the known electronic states of PbF. Section 2.2 provides a brief description of the experimental apparatus used to record spectra. Section 2.3 presents the derived spectroscopic constants. In section 2.4, we discuss implications of our findings.

2.2 Experimental

The spectroscopic constants presented here are derived from spectra obtained using techniques described in Reference [26]. In brief, PbF molecules are produced in an effusive source at 1100K, and spectra are recorded using state-selective, $1 + 1' + 1''$ REMPI. The third harmonic of a 10-Hz neodymium-doped yttrium aluminum garnet (Nd:YAG) laser (Spectra Physics DCR upgraded to a GCR by Larry Wolford Services) pumps a tunable dye laser (Lambda Physik Scanmate IIe). The resulting laser radiation at 436.6 nm excites the $\mathrm{R_{ff}}$ branch of the 1-0 band of the $A \leftarrow X_1$ transition. A second dye laser (Lambda Physik Scanmate IIe) pumped by a harmonic of a Nd:YAG laser (Spectra Physics GCR) produces laser radiation at 780, 476, 446, or 429 nm to further excite the PbF molecule via the $B \leftarrow A$, $D \leftarrow A$, $E \leftarrow A$, or $F \leftarrow A$ transitions, respectively. The molecule is then ionized using a harmonic of the second Nd:YAG laser. The ions are detected by a linear time-of-flight mass spectrometer, and the ion-signal intensity of the $^{206}\mathrm{Pb}^{19}\mathrm{F}$, $^{207}\mathrm{Pb}^{19}\mathrm{F}$, and $^{208}\mathrm{Pb}^{19}\mathrm{F}$ masses are recorded simultaneously as a function of both dye laser frequencies. We were able to observe diffuse spectra via the $C \leftarrow X_1$ transition by $1 + 1'$ REMPI but could not resolve rotational lines. We did not observe the C state using the $1 + 1' + 1''$ technique described, presumably due to a small $C \leftarrow A$ transition dipole moment.

Plots of typical raw data obtained by this method are shown in Figure 2.1. A striking feature of these plots is that the clarity of each branch is immediately apparent.

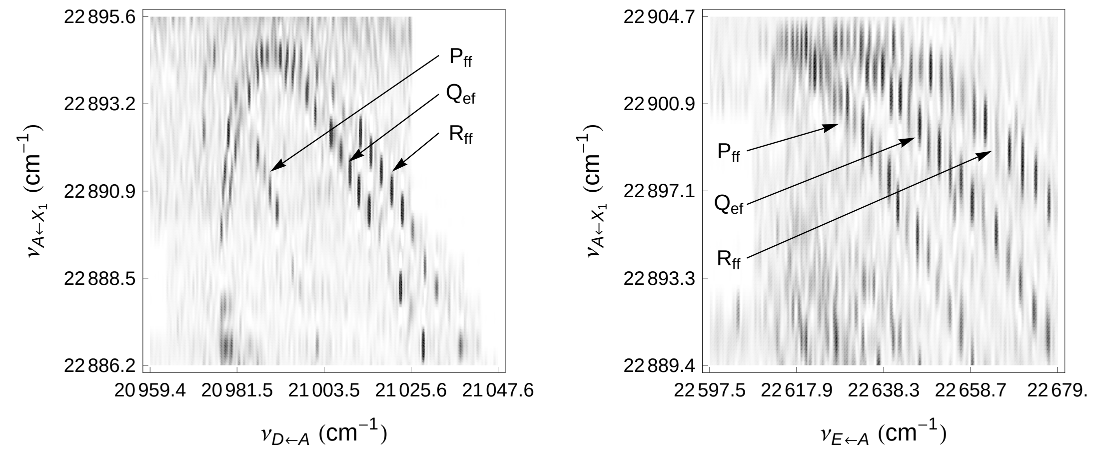

(a)

(b)

Figure 2.1: Raw data of ionization of ^{208}Pb^{19}F by the simultaneous scanning of two laser frequencies. Shown is the R$_{\text{ff}}$ branch of the $A \leftarrow X_1$ transition (vertical direction), and the three branches (from left to right), P$_{\text{ff}}$, Q$_{\text{ef}}$, and R$_{\text{ff}}$, of the excitation through the intermediate state. (a) Ionization signal obtained via the $D \leftarrow A \leftarrow X_1$ transitions. (b) Ionization signal obtained via the $E \leftarrow A \leftarrow X_1$ transitions.

Both plots feature the $\mathrm{R_{ff}}$ branch of the $A \leftarrow X_1$ transition in the vertical direction. The three possible branches, $\mathrm{P_{ff}}$, $\mathrm{Q_{ef}}$, and $\mathrm{R_{ff}}$, of the subsequent excitation through the intermediate state are clearly formed. Because the constants of both the X_1 and A states are already well known [33, 30], the assignment of J for each transition is unambiguous. This greatly simplifies interpretation of the data. In addition, features such as the shifting of the $\mathrm{Q_{ef}}$ branch in the $D \leftarrow A$ transition versus the lack of shifting in the $E \leftarrow A$ transition qualitatively display the relative amount of Ω-doubling in each state.

While this approach is successful for sensitive ionization detection via the D, E, and F states, the background ions from the higher energy photons required to ionize the B state prevented a measurement of the low J lines of the B state by the analogous method. Instead, the B state spectrum was measured with an ion dip method, fixing two laser frequencies to monitor the $D \leftarrow A \leftarrow X_1$ ionization and scanning a third dye laser to excite the $B \leftarrow X_1$ transition. We observe the dip in ionization signal corresponding to the excitation of the $B \leftarrow X_1$ transition. The line positions of the $B \leftarrow X_1$ transitions for the lowest three J values confirm the previously reported value of T_0 [30].

2.3 Observed spectroscopic constants

Rotational lines are recorded at $1/2 < J_{X_1} < 71/2$ and spectra are fitted to

$$\frac{1}{2}\left[F_f(J) + F_e(J)\right] = T_0 + BJ(J+1) - DJ^2(J+1)^2 \tag{2.1}$$

$$\left[F_f(J) - F_e(J)\right] = p(J+1/2) \tag{2.2}$$

using a least squares technique and literature values [30] for A state term values. Here, T_0 is defined such that the lowest energy state of the ground X_1 state is given by

$$U_{X_1}(J = 1/2) = \frac{3}{4}B_{X_1} - \frac{9}{16}D_{X_1} - \frac{1}{2}|p_{X_1}| = 0.102 \text{ cm}^{-1}. \tag{2.3}$$

A summary of the results are presented in Table 2.1. Determination of T_0 of the B state requires both our observations and the spin-rotational constants of Ziebarth [33] and Lumley [30].

2.4 Discussion

2.4.1 The *B*, *E*, and *F* States

Table 2.2 presents a summary of experimentally determined values of T_0 along with the ab initio calculations of Das [35]. All but the E and F states can easily be identified with the calculation. As discussed by Lumley and Barrow [30], the ratio of p/B of the B state is very nearly equal to two, indicating that it is a well isolated $^2\Sigma$ state. We note the missing $F(J = 1/2) \leftarrow A(J = 3/2)$ transition and conclude the value for Ω of the F state must be 3/2. A similar determination of the value of Ω for the E state could not be performed because the lowest rotational lines in the $E \leftarrow A$ transition are too broad to be resolved.

2.4.2 The X_1, X_2, *A*, *C*, and *D* States

The X_2 state has been well characterized as a $^2\Pi_{3/2}$ state by the high resolution study of Ziebarth *et al.* [33]. Our assignment of the symmetry of the C state is both due

Table 2.1: Spectroscopic constants (in cm^{-1}) for the known electronic states of PbF. When three numbers are given, they correspond to the three isotopologues in ascending order, ^{206}Pb^{19}F, ^{207}Pb^{19}F, and ^{208}Pb^{19}F. Otherwise, the average of the three isotopologues is taken.

State		This work			N^a	Previous works			Ref.
X_1	T_0	–				0	0	0	
	B_0	–				0.228208(2)	0.228112(6)	0.228027(2)	[33]
	$10^7 D$	–				1.847(6)	1.82(3)	1.852(6)	
	p	–				-0.138305(5)	-0.13843(1)	-0.138200(6)	
X_2	T_0	–				8275.83885(8)	8275.8327(2)	8275.82358(9)	
	B_0	–				0.233483(2)	0.233385(6)	0.233298(2)	[33]
	$10^7 D$	–				1.788(7)	1.77(3)	1.793(6)	
A	T_0	–				–	–	22502.09(1)	
	B_0	–				–	–	0.20691(4)	[30]
	$10^7 D$	–				–	–	2.23(3)	
	p	–				–	–	0.6185(3)	
B	T_0	35696.78(4)			6	–	–	35696.79(1)	
	B_0	–				–	–	0.24736(5)	[30]
	$10^7 D$	–				–	–	1.62(3)	
	p	–				–	–	[0.4921]	
C	T_0	–				38089			
	B_0	–				–			[29]
	p	–				–			
D	T_0	43866.317(9)	43866.383(7)	43866.450(9)	134	43863			
	B_0	0.24785(4)	0.24779(4)	0.24773(4)		–			[29]
	$10^7 D$	2.2(3)	2.1(3)	1.7(3)		–			
	p	-0.2379(5)	-0.2390(4)	-0.2382(4)		–			
E	T_0	45513.244(7)			133	45415			
	B_0	0.24691(2)				–			[29]
	$10^7 D$	1.3(1)				–			
	p	0.0013(2)				–			
F	T_0	47949.68(2)			26	47927			
	B_0	0.2475(4)				–			[29]
	p	0.015(3)				–			

[a] Number of spectroscopic lines.

Table 2.2: State summary table for ^{208}Pb^{19}F for comparison to theory[a]. Energies are given in units of cm^{-1} and the experimental p/B values are tabulated for $v = 0$ of each electronic state.

State	Experiment			Theory[a]	
	T_0	Symmetry/Ω	p/B	E	Ω
X_1	0	$^2\Pi_{1/2}$ [b]	-0.606	0	1/2
X_2	8275.82358	$^2\Pi_{3/2}$ [b]	0	7832	3/2
A	22502.09	$1/2\,(^2\Sigma^+_{1/2})$[c]	2.989	22820	1/2
B	35696.78	$^2\Sigma^+_{1/2}$ [c]	1.989	37194	1/2
C	38089	$3/2\,(^2\Pi_{3/2})$[d]	–	39817	3/2
D	43866.450	$1/2\,(^2\Pi_{1/2})$[d]	-0.962	45431	1/2
E	45513.244	–	0.005	47036	3/2
F	47949.68	3/2 [d]	0.061	47444	1/2
				48123	1/2
				51002	3/2

[a] Ref. [35]

[b] Ref. [28]

[c] Ref. [30]

[d] This work

to its proximity to the predicted $\Omega = 3/2$ state of Das and because of its interaction with the A and D states as presented in the following discussion. By observing the $D(J = 1/2) \leftarrow A(J = 3/2)$ transition directly, we assign $\Omega = 1/2$ to the D state.

Central to our interpretation of the X_1, A, and D states is the measured value of the ratio of the Ω-doubling parameter, p, to the rotational constant, B. As described by Kopp and Hougen [40], an approximate expression for the ratios of the upper and lower $\Omega = 1/2$ states of an interacting $^2\Pi$ and $^2\Sigma$ pair is given by

$$(p/B)_{\text{upper}} = \pm\{1 - \cos 2\alpha + 2[L(L+1)]^{1/2} \sin 2\alpha\} \tag{2.4a}$$

$$(p/B)_{\text{lower}} = \pm\{1 + \cos 2\alpha - 2[L(L+1)]^{1/2} \sin 2\alpha\}. \tag{2.4b}$$

Here $\cos 2\alpha$ and $\sin 2\alpha$ are given by

$$\cos 2\alpha = \frac{E_\Pi - E_\Sigma - \frac{1}{2}A}{[(E_\Pi - E_\Sigma - \frac{1}{2}A)^2 + A^2 L(L+1)]^{1/2}} \tag{2.5a}$$

$$\sin 2\alpha = \frac{A[L(L+1)]^{1/2}}{[(E_\Pi - E_\Sigma - \frac{1}{2}A)^2 + A^2 L(L+1)]^{1/2}}, \tag{2.5b}$$

where E_Π and E_Σ are the unperturbed energy eigenvalues of the $^2\Pi$ and $^2\Sigma$ states, A is the spin-orbit coupling constant, and L can be treated as a parameter. We assume the Π state to be derived from a p atomic orbital and take $L = 1$. The unperturbed energy eigenvalues are related to the observed energies by

$$E_1 = E_\Pi + \frac{1}{2}A \tag{2.6a}$$

$$E_2 = \frac{1}{2}\left(E_\Pi + E_\Sigma - \frac{1}{2}A\right) + \left[\frac{1}{4}\left(E_\Pi - E_\Sigma - \frac{1}{2}A\right)^2 + \frac{1}{4}A^2 L(L+1)\right]^{1/2} \tag{2.6b}$$

$$E_3 = \frac{1}{2}\left(E_\Pi + E_\Sigma - \frac{1}{2}A\right) - \left[\frac{1}{4}\left(E_\Pi - E_\Sigma - \frac{1}{2}A\right)^2 + \frac{1}{4}A^2 L(L+1)\right]^{1/2} \tag{2.6c}$$

Table 2.3: Experimentally determined and calculated ratios of p/B for two interacting systems.

	p/B			p/B	
	Exp.	Eqs. (2.4–2.6)		Exp.	Eqs. (2.4–2.6)
A	2.989[a]	2.91	X_1	-0.606[b]	-1.16
D	-0.962[c]	-0.91	A	2.989[a]	3.16
C	–		X_2	–	

[a] Ref. [30]
[b] Ref. [33]
[c] This work

where E_1, E_2, and E_3 are the observed energies of the $\Omega = 3/2$ state and $\Omega = 1/2$ states, respectively.

An indication that two states are mixed is evident in the sum of the ratios of their p and B values, i.e. the sum of Equations (2.4a) and (2.4b) gives $|p/B| = 2$. Ratios of p/B for the X_1–X_2–A and A–C–D interacting systems are shown in Table 2.3. It has been previously suggested [30] that the $X_1\,^2\Pi_{1/2}$, $X_2\,^2\Pi_{3/2}$, and $A\,^2\Sigma_{1/2}$ states form an interacting $^2\Pi$ and $^2\Sigma$ pair. However the sum of their respective p/B ratios, $\Sigma(p/B) = 2.38$, agrees less well with this model than the A–D–C sum, $\Sigma(p/B) = 2.03$. Furthermore, the Kopp and Hougen model does more than predict the sum of p/B. By incorporating the energy level spacing of the A–D–C system, the model does a remarkable job of predicting the p/B values of the A and D states. For the same level of agreement with the X_1 and X_2 states, a hypothetical and as-yet unobserved $^2\Sigma_{1/2}$ state at around 48600 cm^{-1} would need to exist. It is interesting to note that although accuracy of the calculations of Das decreases with increasing energy, there is a predicted $\Omega = 1/2$ state near this energy. A further, more complicated, possibility is that all five states form an interacting system.

2.5 Conclusion

We present spectroscopic constants which paint a more complete picture of the electron orbital configuration of the PbF molecule. Our data suggest that the spin-orbit interaction manifested in the X_1–X_2–A system is still not fully understood. This observation may influence new efforts to calculate the sensitivity of PbF to an e-EDM. Precise knowledge of rotational transitions to the B, D, E, and F states may help in development of sensitive detection schemes for PbF ionization.

Chapter 3

Experimental determination of the hyperfine constants of the X_1 and A states of ^{207}Pb^{19}F

The previous chapter establishes the most optimum excitation path through the electronic states of PbF that allows for rotational state resolution of the ground state. Here we push the limits of resolution of the 7 ns pulse width laser system and observe the hyperfine splittings due to the lead nucleus in ^{207}Pb^{19}F (Point ③ on Figure 1.1, pg. 7.)

As appears in Physical Review A, Vol. 78, 054502, 2008, with minor corrections explained in Section 3.5

3.1 Introduction

The predicted sensitivity of the PbF molecule to an electron electric dipole moment (e-EDM) along with its predicted insensitivity to background magnetic fields makes the molecule a promising vehicle with which to study CP-violating Physics [17, 18, 15, 19, 25, 26]. We are involved in an experimental effort that seeks to measure the e-EDM by observing the otherwise degenerate PbF $X_1\,{}^2\Pi_{1/2}(v_{X_1} = 0,\ J_{X_1} = \frac{1}{2},\ F_{X_1},$ $\pm M_{F_{X_1}})$ hyperfine states in a polarizing electric field. This experimental effort relies on calculations that predict the strength of the CP-violating coupling that lifts this degeneracy [41, 17, 18, 15]. One measure of the reliability of these calculations is their ability to predict the effect of the ^{207}Pb nuclear magnetic moment on the energy level structure of the ^{207}Pb^{19}F molecule. Here we report a measurement of the hyperfine energy level structure of ^{207}Pb^{19}F that does not agree with previous prediction [17, 18].

Throughout this work, we ignore the hyperfine interaction of ^{19}F nucleus. To consider the interaction of the ^{207}Pb nucleus, we adopt the parametrization of the hyperfine effect in terms of the hyperfine constants $A_\parallel$ and $A_\perp$ as described elsewhere [41, 15]. In brief, the spin rotational Hamiltonian describing the rotational structure of $^2\Sigma_{1/2}$ and $^2\Pi_{1/2}$ molecules leads to an energy level structure given by

$$U = BJ(J+1) + p(-1)^{J+\frac{1}{2}}\frac{\Delta}{2}\left(J+\frac{1}{2}\right) + U_{HF} \tag{3.1}$$

where

$$U_{HF} = \chi\frac{A_\perp}{4} + q\left(-\tau + s\sqrt{\tau^2 - \frac{1}{4}(A_\parallel - \chi A_\perp)\left\{\left(B-\chi\frac{\Delta}{2}\right) - \frac{1}{4}(A_\parallel - \chi A_\perp)\right\}}\right). \tag{3.2}$$

Here B is the rotational constant of the state and Δ is the spin-orbit parameter, and τ is given by

$$\tau = \left(B - \chi\frac{\Delta}{2}\right)\left(F + \frac{1}{2}\right). \tag{3.3}$$

The remaining parameters p, χ, q, and s are signs with $p = \pm 1$ giving the electronic parity of the state, $\chi = (-1)^F p$, $q = 2(J-F)$, and

$$s = \operatorname{sgn}\left(\tau - \frac{A_\parallel - \chi A_\perp}{8F+4}\right). \tag{3.4}$$

For the case that $s = 1$, Eqs. (3.1)–(3.4) reduce to the result of Kozlov [17]. The resulting energy level structure is shown in Fig. 3.1.

3.2 Experimental

A molecular beam of PbF molecules is produced using methods described previously [25, 26]. A 10-Hz injection seeded neodymium-doped yttrium aluminum garnet (Nd:YAG) laser (Spectra Physics GCR) pumps a dye laser (Spectra Physics PDL II) that is modified to act as a pulsed amplifier for a Toptica diode laser (DL100). The system produces 7 ns pulses of 436.72 nm laser radiation with a bandwidth of 800 MHz (typ.) This pulsed laser radiation in turn excites the $X_1(v_{X_1} = 0, J_{X_1}) \rightarrow A(v_A = 1, J_A)$ transition in PbF. The frequency of the diode laser producing the $X_1 \rightarrow A$ laser radiation varies linearly with time over a range of 10 GHz (typ.) every 100 ms. The frequency of the pulsed laser radiation is tuned by varying the timing of the pulsed dye amplifier system. To calibrate the frequency, a fraction of the diode laser radiation is sent through an etalon (Toptica FPI-100-0500) that is stabilized using a polarization-stabilized helium neon (HeNe) laser (Micro-g LaCoste ML-1.) In an independent measurement, the free-spectral range of this etalon is calibrated by modulating the HeNe laser using an acousto-optic modulator. A wavemeter (Burleigh WA-1000) allows for an absolute frequency calibration of 500 MHz. This scanning strategy allows for relative frequency measurements of lines separated by no more than 15 GHz to be made with an accuracy of 80 MHz.

Lead fluoride molecules excited to the A state are further excited to the D state using pulsed dye laser radiation at 476.99 nm (Spectra-Physics-GCR pumped Lambda Physik Scanmate IIe.) The D-state lead fluoride molecules are then ionized with a pulse of 532 nm laser radiation. The resulting PbF^+ ions are collected using a

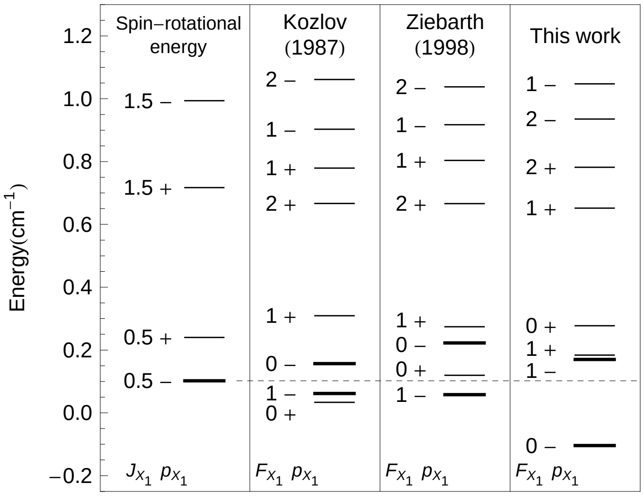

Figure 3.1: Comparison of the energy level diagrams of the hyperfine states of ^{207}Pb^{19}F from Ref. [33], Ref. [17], and this work. The energy levels shown by thicker lines correspond to the two states probed by the $R_1(J_{X_1} = 1/2)$ transition. The dotted line gives the spin-rotational energy of the ground state, ignoring the hyperfine interaction.

time-of-flight mass spectrometer and the ^{206}Pb^{19}F, ^{207}Pb^{19}F, and ^{208}Pb^{19}F signals are simultaneously recorded as a function of the frequency of the $X_1 \to A$ laser radiation. This two-photon excitation scheme is similar to the that described previously [26], but the bandwidth of the pulsed laser radiation driving the $X_1 \to A$ transition has been improved by a factor of 20.

3.3 Analysis

We probe 22 frequency shifts. Specifically R_1 branch transitions with

$$X_1\left(v_{X_1}=0, J_{X_1}, p_{X_1}=(-1)^{J_{X_1}+1/2}\right) \to A\left(v_A=1, J_A=J_{X_1}+1\right) \tag{3.5}$$

and $\frac{1}{2} \leq J_{X_1} \leq \frac{11}{2}$ or $J_{X_1}=\frac{53}{2}$ are measured. In addition the Q_{12} branch transitions with

$$X_1\left(v_{X_1}=0, J_{X_1}, p_{X_1}=(-1)^{J_{X_1}-1/2}\right) \to A\left(v_A=1, J_A=J_{X_1}\right) \tag{3.6}$$

and $\frac{3}{2} \leq J_{X_1} \leq \frac{9}{2}$ are investigated. The combination of R_1 and Q_{12} transitions allows us to differentiate between the X_1- and A-state hyperfine constants. Typical data are shown in Fig. 3.2. This plot gives the isotope-dependent signal of the $R_1(J_{X_1}=11/2)$ transition. For this and every rotational state we observe, the ^{207}Pb^{19}F signal is split into two lines corresponding to transitions obeying the selection rule $\Delta J = \Delta F$. The frequency of the transition starting from $F_{X_1}=J_{X_1}-\frac{1}{2}$ and the transition starting from $F_{X_1}=J_{X_1}+\frac{1}{2}$ are measured with respect to the average energy of the ^{208}Pb^{19}F and ^{206}Pb^{19}F transitions. Because the reduced mass of the isotopes are very nearly the same, this average energy is approximately equal to the energy of the ^{207}Pb^{19}F transition neglecting the hyperfine interaction. However, we do not assume this approximation when analyzing our data. Instead an energy $a_Z J_{X_1} + b_Z$ is subtracted from each frequency shift before it is compared to Eq. (3.2). We then include the parameters a_Z and b_Z in our fit.

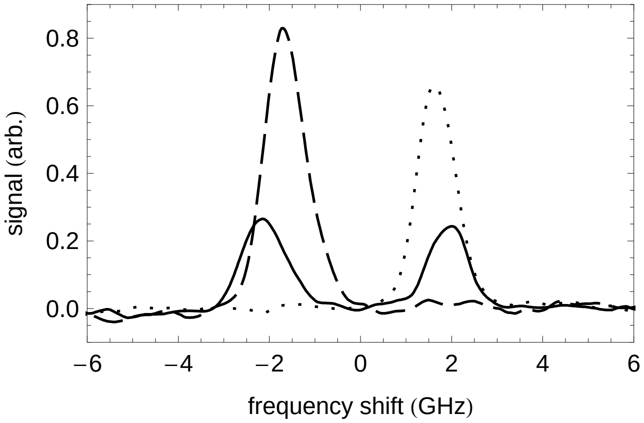

Figure 3.2: Experimentally obtained spectra of the $R_1(J_{X_1} = 11/2)$ line of the $X_1 \rightarrow A$ transition in ^{206}Pb^{19}F(dotted line), ^{207}Pb^{19}F(solid line), and ^{208}Pb^{19}F(dashed line). The zero energy point is taken to be the average transition frequency of the ^{206}Pb^{19}F and ^{208}Pb^{19}F transitions. The ^{207}Pb^{19}F lines correspond to transitions from $F_{X_1} = 6$ (left line) and $F_{X_1} = 5$ (right line.) The relative intensities of the isotope signals do not match the natural abundances of lead because the laser driving the $A \rightarrow D$ transition is fixed during the measurements.

The $R_1(J_{X_1} = 1/2)$ transition shown in Fig. 3.3 is a dramatic demonstration of the disagreement between previous predictions and our experiment. The energy levels of the X_1 states probed in this transition are emphasized by heavy lines in Fig. 3.1. The zero energy point is given by the horizontal dotted line. The spectra of Fig. 3.3 shows

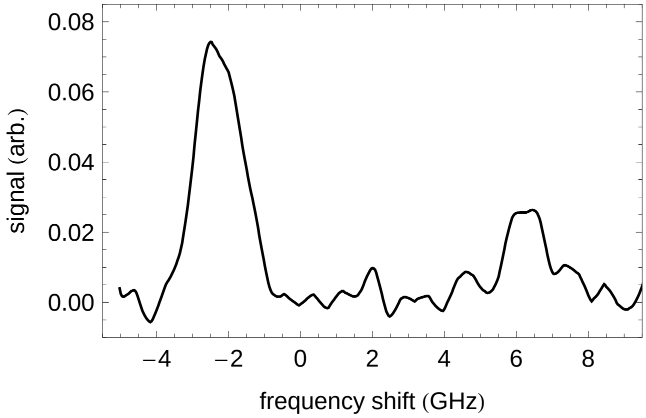

Figure 3.3: Experimentally obtained spectra of the $R_1(J_{X_1} = 1/2)$ line of the $X_1 \to A$ transition in $^{207}\mathrm{Pb}^{19}\mathrm{F}$. The zero energy point is take to be the average transition frequency of the observed (but not shown) $^{206}\mathrm{Pb}^{19}\mathrm{F}$ and $^{208}\mathrm{Pb}^{19}\mathrm{F}$ transitions. The observed lines correspond to transitions from $F_{X_1} = 1$ (left line) and $F_{X_1} = 0$ (right line.)

that the more intense line takes a less energetic photon to excite, indicating that the $F_{X_1} = 1$, $p_{X_1} = -1$ state lies above the $F_{X_1} = 0$, $p_{X_1} = -1$ state. Furthermore, the magnitude of the split is approximately a factor of two bigger than expected from either the prediction of Ziebarth *et al.* [33] or Kozlov *et al.* [17]. This dramatic increase in the hyperfine splitting is only present in the $R_1(J_{X_1} = 1/2)$ transition. However, all of the observed transitions indicate the energy ordering given by the final column of Fig. 3.1. (The exception being the $R_1(J_X = 53/2)$ line which shows two lines of equal intensity to within experimental error.) Furthermore, for every transition observed, the relative intensity between the $F_{X_1} = J_{X_1} + \frac{1}{2}$ transition and the $F_{X_1} = J_{X_1} - \frac{1}{2}$ transition is in quantitative agreement with a simple electric dipole model of line intensities.

To obtain a quantitative fit to the hyperfine constants, we assume the rotational constant $B_{X_1} = 0.228112\ \mathrm{cm}^{-1}$ and spin-orbit constant $\Delta_{X_1} = -0.138413\ \mathrm{cm}^{-1}$ of the X_1 state of $^{207}\mathrm{Pb}^{19}\mathrm{F}$ reported by Fink and coworkers [33]. For the A state, we assume the rotational constant $B_A = 0.20546\ \mathrm{cm}^{-1}$ and spin-orbit constant $\Delta_A = 0.6146\ \mathrm{cm}^{-1}$ of the A state of $^{208}\mathrm{Pb}^{19}\mathrm{F}$ reported by Lumley and Barrow [30]. A chi-squared analysis is performed fitting the 22 observed frequency shifts to the six remaining parameters $A_{\perp,X_1}$, $A_{\parallel,X_1}$, $A_{\perp,A}$, $A_{\parallel,A}$, a_Z and b_Z. The hyperfine constants of the X_1 and A states are listed in Table 3.1 whereas the values $a_Z = -1.0 \pm 1.0$ MHz and $b_z = -28 \pm 30$ MHz are reasonable given the expected mass scaling of both the vibrational and rotational constants of a diatomic molecule.

Table 3.1: Hyperfine constants of the X_1 and A states of $^{207}\mathrm{Pb}^{19}\mathrm{F}$.

	$A_{\perp,X_1}$	$A_{\parallel,X_1}$	$A_{\perp,A}$	$A_{\parallel,A}$
This work[a] (exp.)	7200 ± 150	10300 ± 800	1200 ± 300	3000 ± 2500
Inferred from Ref. [33] (exp.)	$\lvert A_\perp \rvert = 7243 \pm 12$	–	–	–
Ref. [17] (theory)	-7850 ∓ 390	9120 ± 430	–	–
Ref. [18] (theory)	-8990	10990	–	–

[a] Error bars correspond to 90% confidence levels.

Fink and coworkers [33] use a different parametrization of the hyperfine splitting to obtain a hyperfine constant $d = -7243 \pm 12$ MHz for the X_1 state of $^{207}\mathrm{Pb}^{19}\mathrm{F}$. As the rotational constant J_{X_1} increases, the hyperfine splitting of the X_1 state approaches a constant value. From the eigenenergies of Kozlov (Ref. [17], Eq. (3.2)) this value is $|A_{\perp,X_1}/2|$, whereas in the theory employed by Fink this splitting is given by $|d/2|$. Although not explicitly stated, it appears that the value of d obtained by Fink was found by analyzing lines for which J_{X_1} is large enough for this limit to be met. Because our value of $A_{\perp,X_1}$ agrees in magnitude with d, we believe our result is consistent with the experimental data of Fink and coworkers. We are in disagreement, however, in our interpretations of the energy ordering of the X_1 state (see Fig. 3.1.)

An examination of Eqs. (3.1)–(3.4) reveal that the energy level structure depends on $p \cdot A_\perp$ and $p \cdot \Delta$ rather than on $A_\perp$ and Δ. This implies that if the sign of $A_\perp$ and the sign of Δ may be changed together without altering the predicted spectra. Thus our observed energy level structure is evidence that either $A_{\perp,X_1} > 0$ or the electronic parity of both the X_1 and A states (and hence the sign of Δ_{X_1} and Δ_A) have been incorrectly assigned in previous work.

3.4 Conclusion

We have observed a hyperfine-energy-level structure for the ^{207}Pb^{19}F molecule that is markedly different from that of previous predictions. An e-EDM experiment requires the application of a field large enough to mix the ground Ω-doublet states of the PbF molecule. For this reason, the unexpected near degeneracy of the lowest-lying $F = 1$ states of ^{207}Pb^{19}F could be very good news for a PbF based e-EDM experiment: We estimate that this accidental degeneracy will reduce the applied field required to polarize the PbF molecule by one- to two- orders of magnitude. However, our observed energy level structure is evidence that either the predicted value of the hyperfine constant $A_{\perp,X_1}$ is in error, or that the electronic parity assignments of the X_1 and A states are in error. We hope that this surprising revelation motivates renewed theoretical study of the PbF molecule, including its interaction with external magnetic fields and its intrinsic sensitivity to an e-EDM.

3.5 Postscript

The measurement of the hyperfine structure due to the ^{207}Pb nucleas revealed a sign error in the theory of Kozlov and coworkers [17, 15]. This decrepancy was discovered approximately a year after publication of the article presented above. The error was traced to a phase error in the wavefunctions of definite parity. When resolved, the effect was that Equations (3.2) and (3.4) become

$$U_{HF} = -\chi\frac{A_\perp}{4} + q\left(-\tau + s\sqrt{\tau^2 - \frac{1}{4}(A_\parallel + \chi A_\perp)\left\{\left(B - \chi\frac{\Delta}{2}\right) - \frac{1}{4}(A_\parallel + \chi A_\perp)\right\}}\right), \tag{3.7}$$

and

$$s = \operatorname{sgn}\left(\tau - \frac{A_\parallel + \chi A_\perp}{8F + 4}\right). \tag{3.8}$$

The hyperfine constant, $A_\perp$, is negative, in agreement with the theory.

Chapter 4

A capacitively-coupled, floated anode design with application to a reversible electron-ion coincidence time-of-flight detector

In the previous chapters, we have demonstrated an effusive source of PbF as well as developed a REMPI scheme for sensitive detection of the ground X_1 state with rotational and, in the case of ^{207}Pb^{19}F, hyperfine resolution. Though effective, the detection system is inefficient given the duty cycle of the measurement and incapable of resolution of the hyperfine structure due to the fluorine nucleus. Here, a new anode design for use with microchannel plates is presented and incorporated into an electron-ion coincidence detector. This coincidence detector design allows for high-count-rate, single-ion detection. This is suitable for a modified $1 + 1' + 1'$ REMPI scheme which employs a cw laser to drive the first transition and a high repetition rate, high power pulsed laser to drive the remaining transitions to ionization. This new technique, referred to as pseudo-continuous resonance enhanced multiphoton ionization, offers unprecedented resolution in a REMPI scheme, allows the resolution of the hyperfine splittings due to the fluorine nucleus, and corresponds to Point ④ on Figure 1.1 (pg. 7).

4.1 Introduction

In Chapter 2, it was established that the REMPI scheme most sensitive to the ground electronic state is a three photon, two or three color process. The process is as follows: 10-Hz repetition rate, 10-ns time width laser radiation at 436.7 nm drives the valence electron from the electronic ground state (X_1) to the first excited state (A), laser radiation at 476 nm then drives the electron to another excited state (D), and residual laser radiation at 476 nm or additional laser radiation at 532 nm then ionizes the molecule. Although the lifetime of the A state, $\tau \approx 5\,\mu$s [31, 32], is sufficient for resolution of spectral features at the MHz level, the time width of the radiation pulse restricts the experimental resolution to 800 MHz (see Chapter 3). The hyperfine structure could easily be resolved by driving the $A \leftarrow X_1$ transition using a narrow bandwidth, continuous-wave (cw) diode laser. The ionizing laser radiation, though, must remain pulsed due to the high peak power required to ionize the molecule [26].

We halfheartedly attempted to observe REMPI of PbF by driving the $A \leftarrow X_1$ transition using a diode laser and then ionizing using the 10-Hz laser system, but we did not observe any ionization signal. The prospects for success of such an experiment is minimal. This is simply due to the long period of the laser system when compared to the lifetime of the A state. Most of the PbF molecules that are excited to the A state fluoresce to another state before they are excited to the D state and then ionized. The effective duty cycle of this process is $\sim 10^{-5}$.

To ionize the A state of PbF effectively, a radically new approach to REMPI was taken. With the generous support of then University of Oklahoma Vice President for Research Lee Williams, a new laser system (developed for a very different type of experiment) was acquired. This new laser created a new source of 476 nm radiation to drive the $\mathrm{PbF}^+ \leftarrow D \leftarrow A$ transitions. In contrast to the 10-Hz system, this new system has a repetition rate of 76 MHz. Instead of producing pulses that are 10 ns in duration, the new system produces pulses with 6 ps duration. For the expert, this radiation is created as follows: The second harmonic 532 nm laser radiation of a 76-MHz repetition rate, mode-locked neodymium yttrium vanadate (Nd:YVO_4, HighQLaser picoTrain) laser pumps an optical parametric oscillator (OPO, Angewandte Physik und Elektronik Levante Emerald), and the output laser radiation at 864 nm is combined with residual 1064 nm laser radiation of the Nd:YVO_4 laser in a lithium triborate crystal. In the crystal, laser radiation at 476 nm is produced by Type-II sum frequency generation.

This *pseudo-continuous* resonance enhanced multiphoton ionization (pc-REMPI) scheme requires a detection system that can discriminate PbF^+ ion signal from background signal due to non-resonant processes in addition to high single-ion detection rates for sufficient statistics. The detection system described in Chapters 2 and 3 discriminates against background signal by using a mass time-of-flight spectrometer [42, 25, 26, 43]. This spectrometer discriminates PbF^+ ion signal from background signal by synchronizing a pulsed extraction field with the firing of the laser. The ion signal is recorded as a function of delay after the laser shot. Adapting this same method to pc-REMPI is not straight-forward as the 76-MHz repetition rate precludes time discrimination in this way. The expected time of flight of the PbF^+ ion, $t \approx 1\,\mu$s, (see below) is much longer than the period of laser radiation, $\tau = 13\,\text{ns}$. This makes it impossible to discriminate ion signal by correlation with a specific laser pulse.

Ion background discrimination can be achieved by ionizing in a constant, uniform electric field and detecting both the ion and the electron liberated in the process. By correlating electron and ion detection events, referred to as coincidence detection, the time-of-flight of the ion with respect to the electron detection can be measured. In addition to providing mass resolution, this method further discriminates against background ions by requiring both an electron and an ion for a detection event.

In order that electron-ion events be cleanly correlated, the maximum count rate of a single detector must be less than the inverse of the time of flight t_m of an individual ion. This time of flight can, in principle, be made very short by increasing the acceleration field or decreasing the length of the time of flight region. If, however, one makes t_m too small, one looses mass resolution. To put this problem on a quantitative footing, suppose one wishes to distinguish a $^{207}\text{Pb}^{19}\text{F}$ molecule of mass, m, from a $^{208}\text{Pb}^{19}\text{F}$ molecule of mass, $m + \Delta m$. The time of flight of a $^{207}\text{Pb}^{19}\text{F}$ ion, t_m, in the coincidence detector (described later in Section 4.2.2) is proportional to the square root of the mass of the ion.

$$t_m = l_d\sqrt{-\frac{2m}{qV_e}} \tag{4.1}$$

$$= \alpha\sqrt{m} \tag{4.2}$$

where $\alpha = l_d\sqrt{2/(-qV_e)}$ is a constant (cf. Equation (4.8) with $x = 0$, $v_0 = 0$, and

$l_e = l_d$.) The time of flight of the ^{208}Pb^{19}F molecule will then be

$$t_{m+\Delta m} = \sqrt{\frac{m+\Delta m}{m}}\, t_m \tag{4.3}$$

$$\approx t_m + \frac{1}{2}\frac{\Delta m}{m} t_m \tag{4.4}$$

Now suppose that the experimental time resolution of the e^- and PbF$^+$ detection system is given by Δt_d. The requirement that ^{207}Pb^{19}F be distinguished from ^{208}Pb^{19}F implies a minimum time of flight

$$(t_m)_{\min} = \frac{2m}{\Delta m}\Delta t_d \tag{4.5}$$

and, therefore, maximum single-ion collection rate

$$f_{\max} = \frac{1}{(t_m)_{\min}} = \frac{1}{\Delta t_d}\frac{\Delta m}{2m}. \tag{4.6}$$

Blurring of the times of flight of particles of the same mass is typically around 300–500 ps due to misalignment and non-uniformity in the extraction field. Given $\Delta m/2m = 0.002$ and $\Delta t_d = 0.5\,\mathrm{ns}$, the count rate of a single detector must be kept below 1 MHz. In practice, these conditions allow for a count rate of approximately 100 kHz, which is a sufficient data collection rate for an e-EDM experiment. However, if the timing discrimination Δt_d degrades from the sub-nanosecond range, the maximum data collection rate quickly becomes too slow for our desired statistics-limited measurement.

This chapter reviews the care that was taken to assure this level of timing discrimination. In the next section, I will describe a physical design and a numerical model of a fast anode for high single-ion count rates followed by its use in a coincidence detector. Section 4.3 describes an experimental apparatus in which this detector has been used along with typical performance data.

4.2 Detector design

4.2.1 Anode

The design of the anode starts with consideration of the gain medium which amplifies a single ion event to a detectable signal. A microchannel plate (MCP) is a thin glass wafer (0.3 mm) perforated by approximately $10\,\mu$m diameter holes in a closely packed array with conducting layers deposited on the front and rear faces of the plate [44]. Each hole is tilted at an angle of approximately 10° with respect to the faces. These channels in the wafer are treated to be semiconducting to maximize secondary emission and thus act as a electron multipliers. Electrons are emitted inside of a channel upon impact of a charged or neutral particle and are accelerated through the plate by the large electric field formed by a bias voltage applied on the faces ($\approx 1\,$kV). The liberated electrons rattle down the channel in turn freeing more electrons in a cascade effect.

Typically, positive ions are accelerated toward a MCP by applying a large negative voltage to its front face. Upon impact of a single ion, a cascade of electrons is triggered in a channel of the MCP, and a cloud of electrons ($\sim 10^4$) is emitted from the rear of the plate [44]. An anode which is coupled to ground is placed close to the rear of the MCP, and the cloud of electrons which strike the anode is detected by observing the corresponding negative voltage pulse on, for example, an oscilloscope. Negative ion detection presents a difficulty as it requires the anode to be biased at large, positive voltage (see, e.g., Figure 4.4).

Extraction of the signal from a biased anode requires the use of a DC blocking capacitor to decouple the signal from the bias voltage. Careless introduction of the capacitor can cause deformation and degradation of the signal. A typical electron cloud produced from an ion event has a FWHM time width of about 100–200 picoseconds [44]. The high frequencies and small amplitude of the subsequent pulse on the anode make it particularly prone to stray inductance and voltage noise. Many solutions are available including the use of an active filter and/or amplifier [45, 46] or other methods [47, 48] to prevent parasitic inductance and counter noise sources. We found that this difficulty may be overcome by integrating the DC blocking capacitor directly into the anode design as in Reference [49], and optimizing the design to reduce stray inductance.

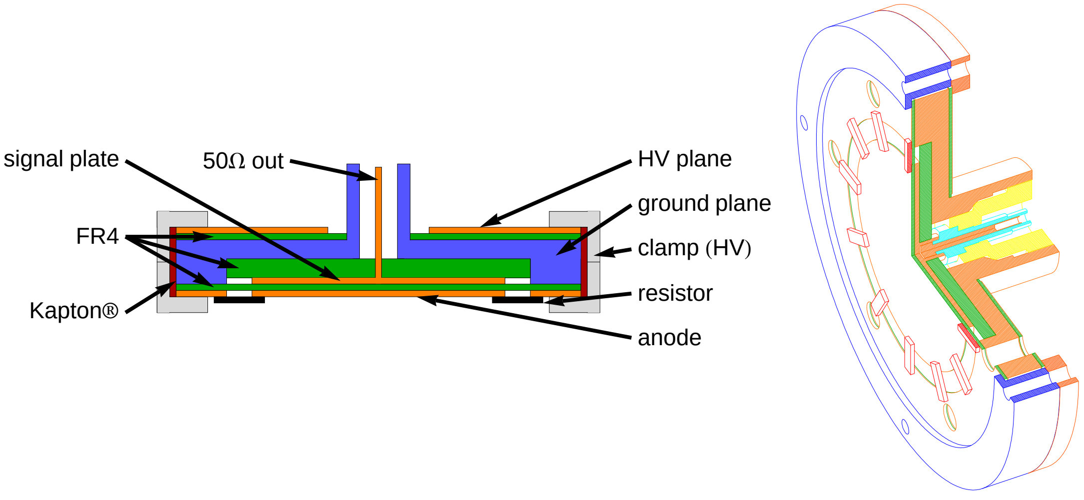

(a) (b)

Figure 4.1: Two cross sections of the integrated anode design. (a) Simplified cross section of the integrated anode design. (b) Projection of a 3D model with cutaway to reveal cross section.

Our design for an anode focuses on maximizing the symmetry of the anode and minimizing sources of inductance by using large, flat conducting surfaces. The design is cylindrically symmetric and consists of the main anode connected to the high voltage shield via surface mount resistors, the signal plate, the inner ground plane, and the signal pin (see Figure 4.1.) The anode and the high voltage shield are constructed of 1/64-inch thick, double-sided copper-clad FR4 circuit board material. A solid copper disk with an indention forms the inner ground plane, and another copper disk forms the signal plate. The spacing between the conducting surfaces is such that the ratio of the capacitances between the high voltage shield and the inner ground plane and the anode and signal plate is approximately 6:1. The capacitance between the main anode and the signal plate is approximately 10 pF. This sandwich is clamped together using a conducting metal, in this case aluminum. Parts of the clamp that are exposed to the inner ground plane are insulated using high dielectric Kapton® tape. Twelve 2.5kΩ surface mount resistors, arranged in a radially symmetric pattern, connect the main anode to the high voltage shield and are soldered in place using a vacuum compatible Silver-Tin solder. The ground plane protrudes through the high voltage shield to provide a connection via coaxial cable to an 50Ω termination.

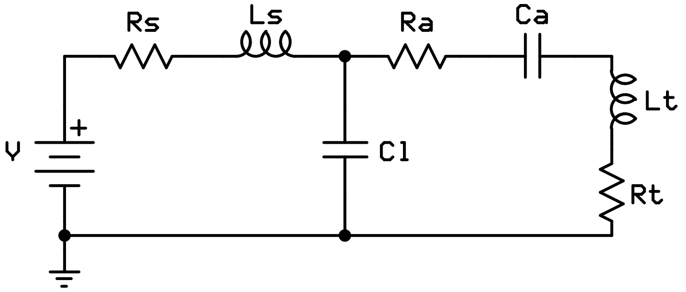

Figure 4.2: Equivalent circuit for the integrated anode.

This anode can be sufficiently described by the equivalent circuit shown in Figure 4.2. Using Kirchhoff's law, the following differential equations describe the circuit.

$$V = (\ddot{Q}_a + \ddot{Q}_l)L_s + (\dot{Q}_a + \dot{Q}_l)R_s + \frac{1}{C_l}Q_l \tag{4.7a}$$

$$\frac{1}{C_l}Q_l = \ddot{Q}_a L_t + \dot{Q}_a(R_a + R_t) + \frac{1}{C_a}Q_a, \tag{4.7b}$$

where Q_a and Q_l are the charges on the anode capacitor, C_a, and the reservoir capacitor, C_l, respectively. V is the bias voltage, R_s and L_s are the resistance and inductance of the voltage source, R_t and L_t are the resistance and inductance of the terminating connection to the oscilloscope, and R_a is the resistance between the two capacitors.

Equations (4.7) are solved numerically for $\dot{Q}_a$ in a time-stepping algorithm to determine the current through the termination resistor, R_t. Charge is added to the anode capacitor, C_a, in a step-wise Gaussian function (FWHM 100 ps) to model the charge cloud from the MCPs incident on the anode. The resulting simulated signal is then convoluted with a Gaussian response function (FWHM 1.04 ns) to account for the 300 MHz bandwidth of the oscilloscope [49]. The program is implemented in *Mathematica*, and results are shown in Figure 4.3 along with a typical electron detection event.

The anode decouples the bias voltage with very little distortion to the signal. The measured signal shows a FWHM of about 1 ns, which corresponds well to the 300 MHz bandwidth of the oscilloscope. This suggests that the pulse width is mostly due to the oscilloscope. Unfortunately, we do not have a larger bandwidth oscilloscope to confirm

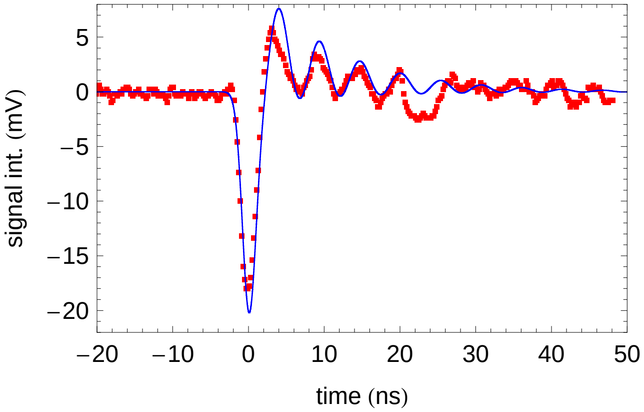

Figure 4.3: Comparison of a typical negative ion event to simulation. A typical stray negative ion peak is shown in red dots. A simulated signal using Equations (4.7) is shown in blue. The following parameters were used in the simulation: $C_a = 10\,\mathrm{pF}$, $R_a = 1\,\mathrm{k\Omega}$, $C_l = 60\,\mathrm{pF}$, $L_s = 12\,\mathrm{nH}$, $R_s = 2\Omega$, $L_t = 60\,\mathrm{nH}$, $R_t = 50\Omega$, and $V = 2400\,\mathrm{V}$.

this. The signal-to-noise of the pulse is approximately 4:1, allowing for sufficient time resolution. It is worth noting that the performance of this anode design is comparable to that of the anode design described in References [50, 49] although it is claimed that this kind of performance is not possible with flat anodes.

4.2.2 Coincidence detector

A particularly useful feature of the integrated anode design is that it may be biased at any voltage, including ground. Positive and negative ions may be detected equally as well, and we take advantage of this to build a symmetric coincidence detector. A simplified schematic of this design is shown in Figure 4.4. The coincidence detector is made of two identical particle detectors. Each detector consists of three basic parts:

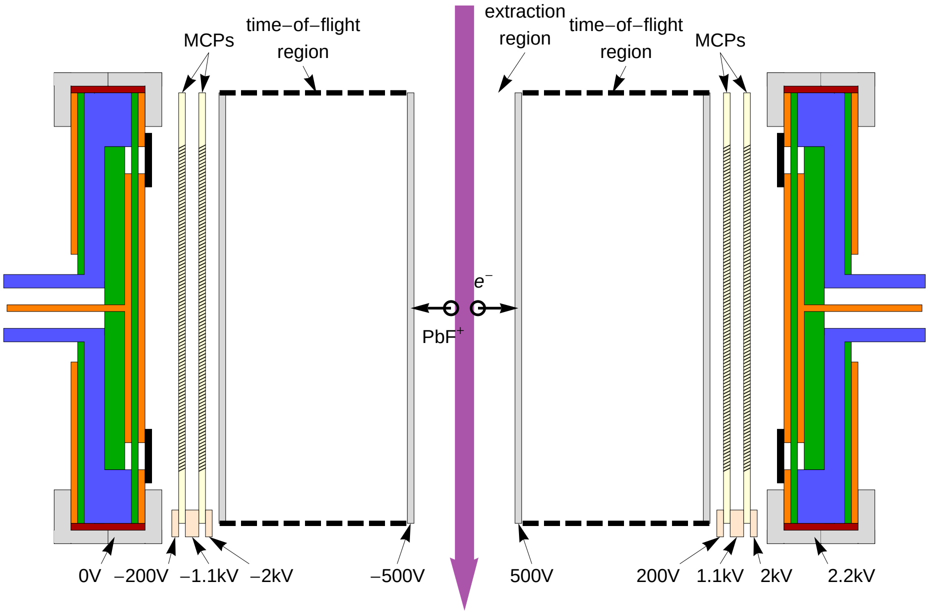

Figure 4.4: Schematic of the coincidence detector with biases and electric field regions labeled. A beam of PbF molecules (out of the page) is crossed by the pc-REMPI laser radiation (purple arrow) at right angles in the center of the detector. The PbF$^+$ ion and electron are then accelerated to the left and right detectors, respectively.

an extraction region, a time-of-flight region, and a detection region. The two detectors share the extraction region. This design allows all of the bias voltages to be reversed to examine systematic errors due to the coincidence detector itself.

The proportions of the detector shown in Figure 4.4 are determined by analyzing the time of flight of charged particles in each detector. The time of flight, t, of a particle of mass, m, from a position, x, from the center of the extraction region to the MCPs is given by

$$t = \frac{l_e m}{2qV_e}\left(v_0 - \sqrt{v_0^2 - \frac{2qV_e}{l_e m}(l_e - 2x)}\right) + \frac{l_d}{\sqrt{v_0^2 - \frac{2qV_e}{l_e m}(l_e - 2x)}} \tag{4.8}$$

where q is the charge of the particle, V_e is the voltage on extraction region plates, l_e is the length of the extraction region, l_d is the length of the time-of-flight region, and v_0 is the initial velocity in the x-direction. Expanding in a Taylor series about $x = 0$, an approximate expression for the time of flight can be written as

$$\tilde{t} \approx t(x=0) - \frac{v_0^2 + \frac{2qV_e}{l_e m}(l_d - l_e)}{\left(v_0^2 - \frac{2qV_e}{m}\right)^{3/2}}\, x + O(x^2) \tag{4.9}$$

Because we are probing a small volume in a molecular beam, v_0 is small. We can see that if we choose the length of the extraction region to be the same length as the drift region, $l_e = l_d$, the first-order term of the time of flight (and the zero-order term in the derivative with respect to position) will be suppressed. The time of flight of particles of the same mass near the center of the detector will be insensitive both position and velocity.

The choice of the extraction region to be the same length as the time-of-flight region eliminates a few of the causes of blurring of times of flight of particles in the detector, but not all. As discussed above, the choice of voltage on the extraction region is made such that the difference of times of flight of adjacent masses is larger than the blurring of timing discrimination. Yet an interesting feature of this geometry is that whatever the choice of extraction field, the ion will arrive at the MCPs with the same energy. This allows for studies of the particle in the presence of many different field strengths. In the case of PbF, the dipole moment of the molecule was determined in this way [51].

4.3 Measurements

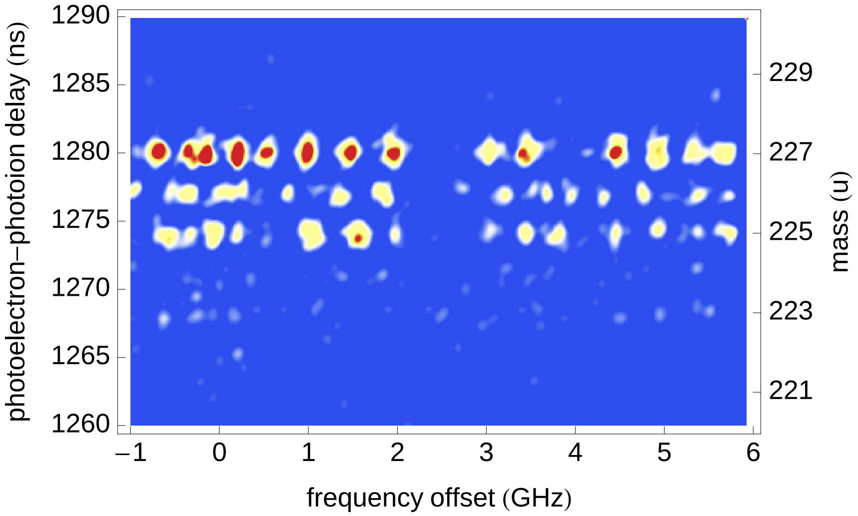

Figure 4.5: Data obtained driving the Q_{ef} branch of the $A(v' = 1) \leftarrow X_1(v = 0)$ transition of PbF. Figure adapted from Reference [36].

The coincidence detector described above has been employed in a pc-REMPI experiment to measure the hyperfine levels of the ground X_1 and first excited A states of PbF [36]. The pc-REMPI detection system is explained in its entirety in

Reference [36]. In brief, a molecular beam of PbF travels at right angles to both the collinear laser radiation and the axis of the detector. The PbF molecules are ionized via pc-REMPI in the center of the detector and form an electron-PbF^+ ion pair. The constant, uniform electric field accelerates the electron and ion in opposite directions where they are then detected (refer to the illustration in Figure 4.4.) The events from both the electron and ion detector are processed by a multi-channel scalar where, after some time discrimination is applied, they are analyzed for coincidence. The coincidence signal is recorded as a function of the frequency of the laser radiation driving the $A \leftarrow X_1$ transition and as a function of the difference between the time of the electron and ion events. Typical data are shown in Figure 4.5. The $A(v = 1) \leftarrow X_1(v = 0)$, $\mathrm{Q_{ef}}$ transitions are well resolved in both frequency and time-of-flight. The peak widths of 40 MHz (FWHM) were obtained, and the isotopologues are well resolved. These data achieve the ultimate goal of fully quantum-state-resolved sensitive and are the first demonstration of hyperfine-resolved REMPI of a molecule sensitive to an e-EDM.

4.4 Conclusion

We have demonstrated an anode design for use with microchannel plates that may be used at any bias voltage. This anode design has been used in the construction of a symmetric and reversible coincidence detector. This detector is optimized for a pseudo-continuous resonance enhanced multiphoton ionization (pc-REMPI) detection scheme that combines the frequency resolution of a cw laser with the sensitivity and discrimination of REMPI-TOF detection.

Chapter 5

Hyperfine constants of the *A* state of PbF

In this chapter, we reexamine data published in Reference [36] with new constants from an upcoming publication [51] to derive new and improved constants of the first excited, A, state of the three dominant isotopologues of PbF. The new data, taken by a collaborative effort in Hannover, Germany, represents the most precise examination of the ground state of PbF to date and corresponds to Point ⑤ on Figure 1.1 (pg. 7).

5.1 Introduction

As discussed in Chapter 1, measurement of an e-EDM requires complete quantum state resolution. Since we employ a pseudo-continuous resonance enhanced multiphoton ionization (pc-REMPI) scheme to detect the molecule [36], the population which we probe with pc-REMPI will be excited through subsequent quantum states. In order to ensure that we are probing the correct quantum state, a complete description of these intermediate quantum states is necessary. The spin-rotational interactions of the X_1 and A states have been established [30, 33, 52] (see Chapter 2.) The hyperfine interactions have only recently been examined correctly and were limited in scope [26, 36] (see Chapter 3.) The study presented in Reference [26] only presents parameters to describe the hyperfine interactions of the electron with the lead nucleus in ^{207}Pb^{19}F. The study of Reference [36] is limited to the hyperfine interactions of the electron with the fluorine nucleus in ^{208}Pb^{19}F. The much weaker ^{206}Pb^{19}F spectra and the highly congested ^{207}Pb^{19}F spectra were not of sufficient quality to make unambiguous line assignments (see Figure 5.1, page 48), and therefore were not analyzed. In this chapter, we resolve this problem by taking advantage of recently determined spectroscopic constants of the X_1 state of PbF [51].

The pc-REMPI detection system presented in the previous chapter was utilized in Reference [36] to determine the fluorine hyperfine constants for the X_1 and A states of ^{208}Pb^{19}F. Although the transitions were well resolved, the previous determination of the hyperfine constants were limited by systematic errors. Neither of the hyperfine constants of the X_1 or A states of ^{208}Pb^{19}F had been determined previous to that study. As discussed in the text of Reference [36], the absolute accuracy of the transitions was limited by the wavemeter used to measure the frequency of the laser radiation. In addition, the transitions were recorded in scans of about 4 GHz, and in order to produce a full spectra, several scans were "patched" together. Determination of the hyperfine constants then required a simultaneous fit of four parameters, two each for the X_1 and A states, to the observed transitions. This lack of absolute accuracy of the transitions introduced systematic error and limited the determination of the constants.

Here we present a reanalysis of data taken in the pc-REMPI experiment. This was made possible by ultra-high resolution data taken recently by a collaboration with the laboratory of Jens-Uwe Grabow. Spectroscopic constants, including hyperfine, of the ground state are derived from this data and are improved by several orders of magnitude over previous determinations [33, 39, 36]. These new constants enable us to calculate the energies of the ground state with high accuracy, and fix these energies for the determination of the A-state constants. This eliminates the systematic errors in determining the absolute positions of the transitions and allows us to rely on the relative accuracy of the transitions which is 10 MHz [36]. The next section briefly describes both experimental apparatuses along with typical data for each. Section 5.3 discusses the analysis used to determine the constants and presents the results of the analysis.

5.2 Experiment

5.2.1 Pseudo-continuous ionization detection

The source of PbF molecules is described in detail in Reference [25]. The previous measurement with pc-REMPI is described in detail elsewhere [36]. To summarize, an effusive molecular beam of PbF travels at right angles to both the collinear laser radiation and the axis of the detector. The PbF molecules are ionized via pc-REMPI ($\mathrm{PbF}^+ \leftarrow D(v'' = 0) \leftarrow A(v' = 1) \leftarrow X_1(v = 0)$) in the center of the detector and form an electron-PbF^+ ion pair. The constant, uniform electric field accelerates the electron and ion in opposite directions where they are then detected (refer to the illustration in Figure 4.4.) The events from both the electron and ion detector are processed by a multi-channel scalar where, after some time discrimination is applied, they are analyzed for coincidence. The coincidence signal is recorded as a function of the frequency of the laser radiation driving the $A \leftarrow X_1$ transition and as a function of the difference between the time of the electron and ion events. Typical integrated data for three mass gates are shown in Figure 5.1.

5.2.2 Fourier transform microwave spectrometer

Measurements of the pure rotational spectra of the ground state of lead monofluoride were conducted in a Fourier transform microwave spectrometer at the Gottfried-Wilhelm-Leibniz Universität, Hannover, Germany. This spectrometer (shown in Figure 5.2) is described in great detail elsewhere [53, 54]. In brief, lead monofluoride is formed by ablating lead in the presence of sulfur hexafluoride. The lead monofluoride passes through a pulsed nozzle via a noble-element carrier gas and expands supersonically into a high vacuum chamber. There, pure rotational transitions in the ground state of PbF are excited by pulsed microwave radiation. The free-induction decay of excited states of PbF are recorded in the time domain in a resonant cavity, and after Fourier transform is applied, observed in the frequency domain. Typical frequency data is shown in Figure 5.3.

5.3 Analysis

Analysis of the recorded transitions requires the calculation of the spin-rotational energies of the X_1 and A states. The spin-rotational energies of the ground, $X_1\,{}^2\Pi_{1/2}$,

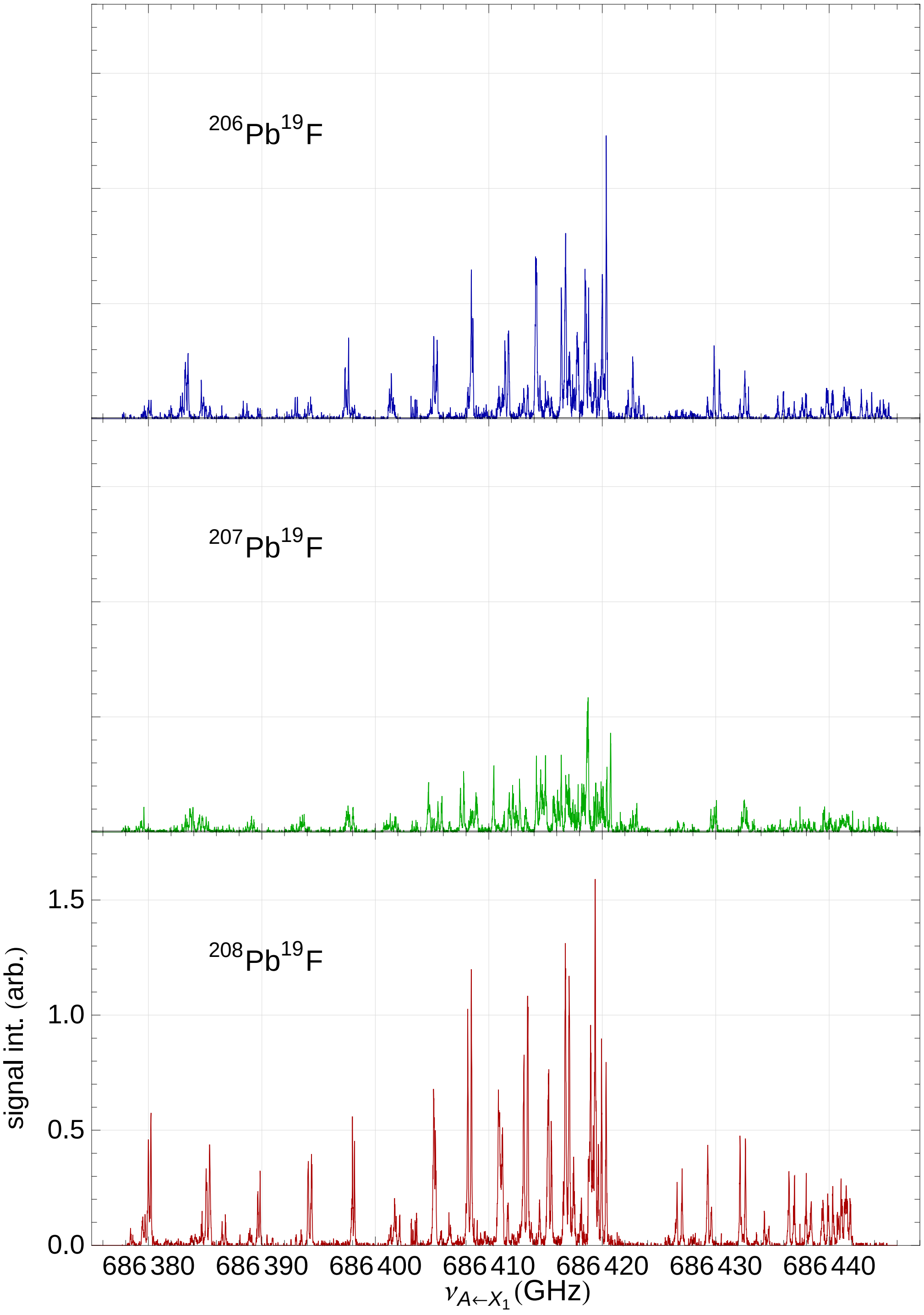

Figure 5.1: Plot of $A(v' = 1) \leftarrow X_1(v = 0)$ transitions of ^{206}Pb^{19}F, ^{207}Pb^{19}F, and ^{208}Pb^{19}F detected by pc-REMPI.

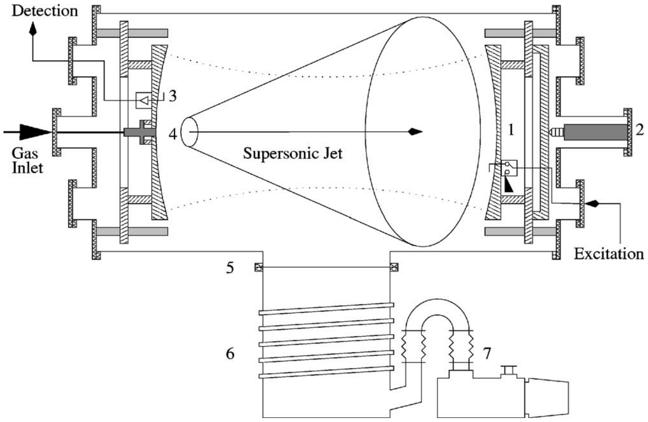

Figure 5.2: Microwave spectrometer. Labeled components are (1) aluminum mirrors; (2) motorized micrometer; (3) microwave antenna; (4) solenoid-actuated, laser ablation nozzle; (5) stainless-steel vacuum chamber; (6) diffusion pump; and (7) mechanical pump. Figure adapted from Reference [54].

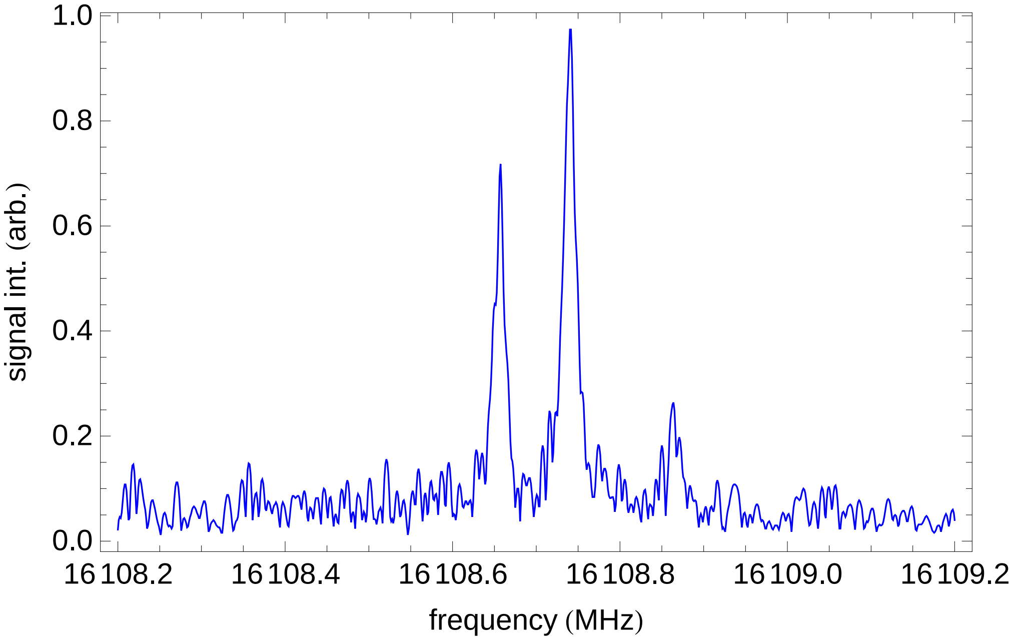

Figure 5.3: Typical data from the microwave spectrometer. This data shows the excitation of the ($J = 5/2$, $F = 5/2$, $p_s = -1$) level of the X_1 state of $^{207}\mathrm{Pb}^{19}\mathrm{F}$.

state are calculated from the lower eigenvalue of the following Hamiltonian [55, 56, 57],

$$\begin{aligned}\mathbf{H}_{rot}(J,p_s) = &\begin{bmatrix} \frac{A}{2} + \left(B + \frac{\tilde{A}_D}{2}\right) z & -B\sqrt{z} \\ -B\sqrt{z} & -\frac{A}{2} + \left(B - \frac{\tilde{A}_D}{2}\right)(z+2) \end{bmatrix} \\ &+ \frac{p_s}{2}(-1)^{J+1/2}\left(J + \frac{1}{2}\right) \begin{bmatrix} 0 & -\frac{p_D}{2}\sqrt{z} \\ -\frac{p_D}{2}\sqrt{z} & p + p_D(z+2) \end{bmatrix} \\ &+ \begin{bmatrix} \tilde{A}_H\, z^2 - D\, z(z+1) & 2D\sqrt{z}(z+1) + \tilde{A}_H\sqrt{z} \\ 2D\sqrt{z}(z+1) + \tilde{A}_H\sqrt{z} & \tilde{A}_H(z+2)^2 - D(z+1)(z+4) \end{bmatrix}\end{aligned} \tag{5.1}$$

Here, B is the rotational parameter; D is the correction to the rotational parameter due to centrifugal distortion; p is Ω-doubling parameter; p_D is the centrifugal correction to the Ω-doubling parameter; A is the spin-orbit parameter; $\tilde{A}_D$ is the spin-orbit dependent correction to B; $\tilde{A}_H$ is the spin-orbit dependent correction to D, p_s is the total parity of the electronic state, and z is defined as $z = (J + 1/2)^2 - 1$.

The spin-rotational energies of the first excited, A, state are given by [40, 57, 52]

$$\begin{aligned}U_{rot}(J,F,p_s) = &\; T_\nu + B\, J(J+1) - D\, J^2(J+1)^2 \\ &+ \frac{p_s}{2}(-1)^{J+1/2}\left(p\left(J+\frac{1}{2}\right) + p_D\left(J+\frac{1}{2}\right)^3\right)\end{aligned} \tag{5.2}$$

where T_ν is the electronic and vibrational energy term.

The hyperfine interactions in both the X_1 and A states are given by the eigenvalues of the following matrices. The energies of the ^{206}Pb^{19}F and ^{208}Pb^{19}F isotopologues are given by eigenvalues of the 2 × 2 matrix,

$$\mathbf{H}_{HF,even} = \begin{bmatrix} -\frac{\chi\, ^1A_\perp}{4} - \frac{^1A_\chi}{4(2F+1)} & ^1A_\chi\frac{\sqrt{F(F+1)}}{2(2F+1)} \\ ^1A_\chi\frac{\sqrt{F(F+1)}}{2(2F+1)} & -\frac{\chi\, ^1A_\perp}{4} + \frac{^1A_\chi}{4(2F+1)} \end{bmatrix}, \tag{5.3}$$

where $\chi = (-1)^{F-1/2}\, p_s$ and ${}^1A_\chi = {}^1A_\parallel + \chi\, {}^1A_\perp$. The energies of the ${}^{207}\mathrm{Pb}{}^{19}\mathrm{F}$ isotopologue are given by eigenvalues of the 4×4 matrix,

$$\mathbf{H}_{HF,odd} =$$

$$\begin{bmatrix} 0 & -\frac{2F\chi\underline{A}_\perp + \underline{A}_\chi}{4\sqrt{F(F+1)}} & \sqrt{\frac{2F+3}{F+1}}\frac{2\chi\underline{A}_\perp - \underline{A}_\chi}{4} & \frac{\underline{A}_\chi}{4}\sqrt{\frac{2F-1}{F}} \\ -\frac{2F\chi\underline{A}_\perp + \underline{A}_\chi}{4\sqrt{F(F+1)}} & -\frac{2F\chi\overline{A}_\perp + \overline{A}_\chi}{4F(F+1)} & \frac{-2\chi\overline{A}_\perp + \overline{A}_\chi}{4}\sqrt{\frac{(2F+3)F}{(F+1)^2}} & \frac{\overline{A}_\chi}{4}\sqrt{\frac{(F+1)(2F-1)}{F^2}} \\ \sqrt{\frac{2F+3}{F+1}}\frac{2\chi\underline{A}_\perp - \underline{A}_\chi}{4} & \frac{-2\chi\overline{A}_\perp + \overline{A}_\chi}{4}\sqrt{\frac{(2F+3)F}{(F+1)^2}} & \frac{2(F+2)\chi\overline{A}_\perp - \overline{A}_\chi}{4(F+1)} & 0 \\ \frac{\underline{A}_\chi}{4}\sqrt{\frac{2F-1}{F}} & \frac{\overline{A}_\chi}{4}\sqrt{\frac{(F+1)(2F-1)}{F^2}} & 0 & \frac{-2F\chi\overline{A}_\perp + \overline{A}_\chi}{4F} \end{bmatrix}. \tag{5.4}$$

Here we define

$$\overline{A}_\parallel = \frac{1}{2}\left({}^1A_\parallel + {}^2A_\parallel\right), \tag{5.5a}$$

$$\underline{A}_\parallel = \frac{1}{2}\left({}^1A_\parallel - {}^2A_\parallel\right), \tag{5.5b}$$

$$\overline{A}_\perp = \frac{1}{2}\left({}^1A_\perp + {}^2A_\perp\right), \tag{5.5c}$$

$$\underline{A}_\perp = \frac{1}{2}\left({}^1A_\perp - {}^2A_\perp\right), \tag{5.5d}$$

$$\overline{A}_\chi = \frac{1}{2}\left(\overline{A}_\parallel + \chi\overline{A}_\perp\right), \tag{5.6a}$$

$$\underline{A}_\chi = \frac{1}{2}\left(\underline{A}_\parallel - \chi\underline{A}_\perp\right), \tag{5.6b}$$

$$\chi = (-1)^{F-1/2}\, p_s \tag{5.6c}$$

The parameters used in the calculation of the energies of the $X_1(v = 0)$ and $A(v = 1)$ states are given in Tables 5.1 and 5.2, respectively. The spin-rotational constants for the $A(v = 1)$ state are available for ${}^{208}\mathrm{Pb}{}^{19}\mathrm{F}$ [30]. For ${}^{206}\mathrm{Pb}{}^{19}\mathrm{F}$ and ${}^{207}\mathrm{Pb}{}^{19}\mathrm{F}$, the constants are mass scaled. The energies of the X_1 state and the spin-rotational energies of the A state were held fixed, and the hyperfine constants were fitted by a least-squares minimization algorithm. The values of ${}^1A_\perp$ and ${}^1A_\parallel$ of ${}^{207}\mathrm{Pb}{}^{19}\mathrm{F}$ did not differ significantly from the average of those values for ${}^{206}\mathrm{Pb}{}^{19}\mathrm{F}$ and ${}^{208}\mathrm{Pb}{}^{19}\mathrm{F}$.

Table 5.1: Spectroscopic constants of the ground X_1 state of the three dominant isotopologues of PbF.

	Molecule		
Parameter	^{206}Pb^{19}F	^{207}Pb^{19}F	^{208}Pb^{19}F
A	248,117,208.(3)[a]	248,117,012.(2)[b]	248,116,742.(2)[b]
$\tilde{A}_H$	0.000089(2)[a]	0.0000899(3)[a]	0.0000896(6)[b]
$\tilde{A}_D$	157.7238(60)[a]	157.6728(30)[b]	157.5957(40)[b]
B	6,920.7281(1)[b]	6,917.9139(10)[b]	6,915.1146(20)[b]
D	0.00545(2)[a]	0.00554(2)[b]	0.005477(7)[b]
p	–4,146.9284(2)[b]	–4,145.2272(4)[b]	–4.143.5493(4)[b]
p_D	–0.0036(1)[a]	–0.00368(5)[b]	–0.00312(3)[b]
$^1A_\parallel$	409.905(2)[b]	409.90701[b]	409.909(2)[b]
$^1A_\perp$	255.9897(8)[b]	255.99272[b]	255.9958(8)[b]
$^2A_\parallel$	–	10,146.662(2)[b]	–
$^2A_\perp$	–	–7,264.065(5)[b]	–

[a] Reference [33]

[b] Reference [51]

Table 5.2: Spectroscopic constants of the $A(v = 1)$ state of the three dominant isotopologues of PbF. All parameters are given in units of MHz.

	Molecule		
Parameter	^{206}Pb^{19}F	^{207}Pb^{19}F	^{208}Pb^{19}F
B	6,164.53(1)	6,161.80(1)[a]	6,159.54(1)[b]
D	0.007(1)[a]	0.007(1)[a]	0.007(1)[b]
p	18,440.(2)[a]	18,433.(1)[a]	18,425.(1)[b]
p_D	0.03(1)[a]	0.03(1)[a]	0.03(1)[b]
T_1	686,432.8(2)	686,437.6(2)	686,429.4(1)[b]

[a] Mass scaled from Ref. [30]

[b] Ref. [30]

Therefore these two values were held fixed to allow for a more accurate determination of the parameters $^2A_\perp$ and $^2A_\parallel$. The results are presented in Table 5.3 along with the electronic energy, T_1, of each isotopologue.

Table 5.3: Hyperfine constants for the $A(v = 1)$ state of the isotopologues of lead monofluoride. All parameters are given in units of GHz.

	Molecule		
Parameter	^{206}Pb^{19}F	^{207}Pb^{19}F	^{208}Pb^{19}F
$^1A_\perp$	–0.79(3)	–0.79[a]	–0.79(2)
$^1A_\parallel$	1.56(9)	1.61[a]	1.66(7)
$^2A_\perp$	–	1.46(4)	–
$^2A_\parallel$	–	2.8(1)	–

[a] Value fixed during fit.

[b] Ref. [30]

5.4 Conclusion

The Fourier transform microwave spectrometer has probed the X_1 state of PbF in unprecedented detail. This allows for the analysis of data reported in Reference [36]. The analysis, presented in this chapter, has resulted in improved hyperfine constants for the $A(v = 1)$ state of ^{208}Pb^{19}F, and the first reported hyperfine constants for the $A(v = 1)$ state of ^{206}Pb^{19}F and ^{207}Pb^{19}F.

Chapter 6

Summary and Conclusion

Sandars proposal in the 1970s to use molecules to measure the e-EDM [12] has gained an enormous amount of enthusiasm in the last decade. With the conclusion of the Thallium atomic beam experiment [8], many groups [58, 59, 16, 60, 61, 62], including our own group, are looking to diatomic molecules to push the measurement of the e-EDM further. At the beginning of this work, lead monofluoride was only a theoretically promising candidate. To prepare for a measurement of the e-EDM with PbF, we set out with three goals in mind. The first was to test the theory behind the calculated sensitivity of PbF to the e-EDM. The second was to learn how PbF behaves in external electric and magnetic fields. The third was to devise a method to attain complete state-selective detection of PbF. In the span of this work, we accomplished all three of these goals.

The initial tests of the theory were made by the study presented in Chapter 2. Specifically, we discovered that the electronic state mixing was far different than previously determined (see Section 2.4.2.) The sensitivity of PbF to an e-EDM depends critically on the wavefunction density at the nuclei of the molecule. This relativistic interaction is directly responsible for the lifting of the time-symmetric, quantum-state degeneracy [63, 12] and would be greatly suppressed in a pure, unmixed $^2\Pi$ state [64, 17]. The calculations of the sensitivity of PbF to the e-EDM by Kozlov and coworkers [17, 15] were based on measurements and analysis made by Lumley and Barrow in 1977 [30]. In their analysis, they described the departure of the ground state from pure $^2\Pi$ character using the model of Kopp and Hougen [40] and hypothesized that this departure was due to electronic mixing with the nearest $^2\Sigma$ state. Our findings evidence a much different picture of electronic state interactions. Fortunately, we do not expect the sensitivity of PbF to the e-EDM to change due to this new found state mixing [65]. Our examination of the excited states of PbF provide theorists with a more complete picture of the molecule and will allow for more accurate determinations of the sensitivity of PbF to the e-EDM.

We established the response of PbF to external fields by the measurement of the hyperfine parameters, presented in Chapters 3 and 5. In pure electric and magnetic fields, the quantum states of the electron are states of definite parity. Therefore, it was crucial to confirm the parity assignments of the quantum states of PbF. We discovered an energy level ordering of the ground ro-vibrational state of ^{207}Pb^{19}F in direct contradiction to the literature [15, 33, 39] (see Section 3.3.) This led to two important consequences: The revelation of a twenty-year-old sign error that had been lurking in the theory of Kozlov and coworkers [36]; and the correction of the prediction, based on the same flawed theory, that the g-factor becomes zero at a specific electric field [19, 36]. With the parity of all of the quantum states established, we were able, in collaboration with Dr. Jens-Uwe Grabow, to both confirm this energy level structure and measure the interaction of the ground state with electric and magnetic fields to high precision [51].

Lastly, we developed a novel technique to state-selectivity detect PbF, as presented in Chapter 4. The technique of pc-REMPI with coincidence detection achieves high frequency and mass resolution with high single-ion count rates and provides us with complete quantum-state-selective detection of PbF [36].

The results of this work encompass and complete the preliminary studies of lead monofluoride and its suitability as a molecule with which to measure the *e*-EDM. Lead monofluoride is now established on both theoretical and experimental grounds as a strong candidate, and our laboratory is ready for the first stages of a measurement of the *e*-EDM.

References

[1] E. Purcell and N. Ramsey, Phys. Rev. **78**, 807 (1950).

[2] A. Sakharov, Pisma Zh. Eksp. Teor. Fiz. **5**, 32 (1967).

[3] J. H. Christenson, J. W. Cronin, V. L. Fitch, and R. Turlay, Phys. Rev. Lett. **13**, 138 (1964).

[4] R. Arnowitt, B. Dutta, and Y. Santoso, Phys. Rev. D **64**, 113010 (2001).

[5] F. Hoogeveen, Nucl. Phys. B **341**, 322 (1990).

[6] K. Abdullah, C. Carlberg, E. D. Commins, H. Gould, and S. B. Ross, Phys. Rev. Lett. **65**, 2347 (1990).

[7] E. D. Commins, S. B. Ross, D. DeMille, and B. C. Regan, Phys. Rev. A **50**, 2960 (1994).

[8] B. C. Regan, E. D. Commins, C. J. Schmidt, and D. DeMille, Phys. Rev. Lett. **88**, 071805 (2002).

[9] D. Bourilkov, Phys. Rev. D **64**, 071701 (2001).

[10] G. Gabrielse, D. Hanneke, T. Kinoshita, M. Nio, and B. Odom, Phys. Rev. Lett. **97**, 030802 (2006).

[11] P. G. H. Sandars and E. Lipworth, Phys. Rev. Lett. **13**, 718 (1964).

[12] P. Sandars, At. Phys. **14**, 71 (1975).

[13] P. G. H. Sandars, Phys. Rev. Lett. **19**, 1396 (1967).

[14] I. B. Khriplovich and S. K. Lamoreaux, *CP Violation Without Strangeness: Electric Dipole Moments of Particles, Atoms, and Molecules* (Springer-Verlag, Berlin, 1997).

[15] M. G. Kozlov and L. N. Labzowsky, J. Phys. B: At. Mol. Opt. Phys. **28**, 1933 (1995).

[16] E. R. Meyer and J. L. Bohn, Phys. Rev. A **78**, 010502 (2008).

[17] M. G. Kozlov, V. I. Fomichev, Y. Y. Dmitriev, L. N. Labzovsky, and A. V. Titov, J. Phys. B: At. Mol. Phys. **20**, 4939 (1987).

[18] Y. Y. Dmitriev, Y. G. Khait, M. G. Kozlov, L. N. Labzovsky, A. O. Mitrushenkov, A. V. Shtoff, and A. V. Titov, Phys. Lett. A **167**, 280 (1992).

[19] N. E. Shafer-Ray, Phys. Rev. A **73**, 034102 (2006).

[20] P. M. Johnson and C. E. Otis, Ann. Rev. Phys. Chem. **32**, 139 (1981).

[21] K. Kimura, International Reviews in Physical Chemistry **6**, 195 (1987).

[22] M. N. R. Ashfold and J. D. Howe, Ann. Rev. Phys. Chem. **45**, 57 (1994).

[23] D. Feldman, R. Lengel, and R. Zare, Chemical Physics Letters **52**, 413 (1977).

[24] R. J. Van Zee, M. L. Seely, T. C. DeVore, and W. Weltner, Jr., J. Chem. Phys. **82**, 1192 (1978).

[25] C. P. McRaven, P. Sivakumar, and N. E. Shafer-Ray, Phys. Rev. A **75**, 024502 (2007).

[26] P. Sivakumar, C. P. McRaven, D. Combs, and N. E. Shafer-Ray, Phys. Rev. A **77**, 062508 (2008).

[27] F. Morgan, Phys. Rev. **49**, 47 (1936).

[28] G. D. Rochester, Proceedings of the Royal Society of London. Series A, Mathematical and Physical Sciences **153**, 407 (1936).

[29] G. D. Rochester, Proceedings of the Royal Society of London. Series A, Mathematical and Physical Sciences **167**, 567 (1938).

[30] D. J. W. Lumley and R. F. Barrow, J. Phys. B: Atom. Molec. Phys. **10**, 1537 (1977).

[31] J. Chen and P. J. Dagdigian, J. Chem. Phys. **96**, 1030 (1992).

[32] O. Shestakov, A. M. Pravilov, H. Demes, and E. H. Fink, Chem. Phys. **165**, 415 (1992).

[33] K. Ziebarth, K. D. Setzer, O. Shestakov, and E. H. Fink, J. Mol. Spectrosc. **191**, 108 (1998).

[34] K. Balasubramanian, J. Chem. Phys. **83**, 2311 (1985).

[35] K. K. Das, I. D. Petsalakis, H.-P. Liebermann, A. B. Alekseyev, and R. J. Buenker, J. Chem. Phys. **116**, 608 (2002).

[36] P. Sivakumar, C. P. McRaven, P. M. Rupasinghe, T. Z. Yang, N. E. Shafer-Ray, T. J. Sears, and G. E. Hall, Mol. Phys. **108**, 927 (2010).

[37] N. E. Shafer-Ray, K. A. Milton, B. R. Furneaux, E. R. I. Abraham, and G. R. Kalbfleisch, Phys. Rev. A **67**, 045401 (2003).

[38] M. Rupasinghe and N. E. Shafer-Ray, Phys. Rev. A **78**, 033427 (2008).

[39] C. P. McRaven, P. Sivakumar, and N. E. Shafer-Ray, Phys. Rev. A **78**, 054502 (2008).

[40] I. Kopp and J. T. Hougen, Can. J. Phys. **45**, 2581 (1967).

[41] M. G. Kozlov, Zh. Eksp. Teor. Fiz. [Sov. Phys. JETP] **89**, 1933 (1985).

[42] W. C. Wiley and I. H. McLaren, Rev. Sci. Instrum. **26**, 1150 (1955).

[43] P. Sivakumar, Ph.D. thesis, University of Oklahoma, 2010.

[44] J. L. Wiza, Nucl. Instrum. Methods **162**, 587 (1979).

[45] S.-H. Seo, H.-Y. Chang, and S. K. Kim, Rev. Sci. Instrum. **67**, 4120 (1996).

[46] P. Schwartze, H. Baumgartel, and C. G. Eisenhardt, Rev. Sci. Instrum. **72**, 3125 (2001).

[47] A. Stolow, Rev. Sci. Instrum. **67**, 1777 (1996).

[48] P. Wurz and R. Schletti, Rev. Sci. Instrum. **72**, 3225 (2001).

[49] P. Wurz and L. Gubler, Rev. Sci. Instrum. **67**, 1790 (1996).

[50] P. Wurz and L. Gubler, Rev. Sci. Instrum. **65**, 871 (1994).

[51] R. Mawhorter, T. J. Sears, T. Z. Yang, P. M. Rupasinghe, C. P. McRaven, N. Shafer-Ray, and J.-U. Grabow, Phys. Rev. A (in prep.).

[52] C. P. McRaven, P. Sivakumar, N. E. Shafer-Ray, G. E. Hall, and T. J. Sears, J. Mol. Spectrosc. **262**, 89 (2010), accepted May 25, 2010.

[53] M. Schnell, D. Banser, and J.-U. Grabow, Rev. Sci. Instrum. **75**, 2111 (2004).

[54] J.-U. Grabow, E. S. Palmer, M. C. McCarthy, and P. Thaddeus, Rev. Sci. Instrum. **76**, 093106 (2005).

[55] J. M. Brown, E. A. Colbourn, J. K. G. Watson, and F. D. Wayne, Journal of Molecular Spectroscopy **74**, 294 (1979).

[56] C. Amiot, J. P. Maillard, and J. Chauville, Journal of Molecular Spectroscopy **87**, 196 (1981).

[57] J. M. Brown and A. Carrington, *Rotational Spectroscopy of Diatomic Molecules* (Cambridge University Press, Cambridge, 2003).

[58] J. J. Hudson, B. E. Sauer, M. R. Tarbutt, and E. A. Hinds, Phys. Rev. Lett. **89**, 023003 (2002).

[59] A. N. Petrov, N. S. Mosyagin, T. A. Isaev, and A. V. Titov, Phys. Rev. A **76**, 030501 (2007).

[60] S. Bickman, P. Hamilton, Y. Jiang, and D. DeMille, Phys. Rev. A **80**, 023418 (2009).

[61] J. Lee, E. Meyer, R. Paudel, J. Bohn, and A. Leanhardt, J. Mod. Opt. **56**, 2005 (2009).

[62] H. Loh, R. Stutz, M. Grau, and E. Cornell, in *Bulletin of the American Physical Society: 41st Annual Meeting of the APS Division of Atomic, Molecular and Optical Physics* (American Physical Society, Houston, Texas, 2010), No. 5, p. M1.127.

[63] P. Sandars, Phys. Lett. **14**, 194 (1965).

[64] R. A. Frosch and H. M. Foley, Phys. Rev. **88**, 1337 (1952).

[65] M. G. Kozlov, (private communication).